

1 **Uranium isotope evidence for two episodes of deoxygenation during Oceanic Anoxic Event 2**

2

3 **Author List**

4 Matthew O. Clarkson<sup>a,1,2</sup>, Claudine H. Stirling<sup>a</sup>, Hugh C. Jenkyns<sup>b</sup>, Alexander J. Dickson<sup>b,c</sup>, Don Porcelli<sup>b</sup>,

5 Christopher M. Moy<sup>d</sup>, Philip A.E. Pogge von Strandmann<sup>e</sup>, Ilsa R. Cooke<sup>a</sup> and Timothy M. Lenton<sup>f</sup>

6

7 ***Published in the Proceedings of the National Academy of Sciences (PNAS), March 5 2018***

8 ***[www.pnas.org/cgi/doi/10.1073/pnas.1715278115](http://www.pnas.org/cgi/doi/10.1073/pnas.1715278115)***

9

10 **Affiliations**

11 *<sup>a</sup> Department of Chemistry, University of Otago, P.O. Box 56, Dunedin 9054, New Zealand*

12 *<sup>b</sup> Department of Earth Sciences, University of Oxford, South Parks Road, Oxford OX1 3AN, UK*

13 *<sup>c</sup> Department of Earth Sciences, Royal Holloway University of London, Egham, Surrey, TW20 0EX, UK*

14 *<sup>d</sup> Department of Geology, University of Otago, P.O. Box 56, Dunedin 9054, New Zealand*

15 *<sup>e</sup> London Geochemistry and Isotope Centre (LOGIC), Institute of Earth and Planetary Sciences,*

16 *University College London and Birkbeck, University of London, Gower Street, London WC1E 6BT, UK*

17 *<sup>f</sup> Earth System Science, College of Life and Environmental Sciences, University of Exeter, Exeter EX4*

18 *4QE, UK*

19

20 *<sup>1</sup>To whom correspondence should be addressed. Email: [matthew.clarkson@erdw.ethz.ch](mailto:matthew.clarkson@erdw.ethz.ch)*

21 *<sup>2</sup> Present address: Institute of Geochemistry and Petrology, Department of Earth Sciences, ETHZ, 8092,*

22 *Zurich, Switzerland*

23

24

25

26

27 **Abstract**

28 Oceanic Anoxic Event 2 (OAE 2), occurring ~94 million years ago, was one of the most extreme carbon  
29 cycle and climatic perturbations of the Phanerozoic Eon. It was typified by a rapid rise in atmospheric  
30 CO<sub>2</sub>, global warming, and marine anoxia, leading to the widespread devastation of marine ecosystems.  
31 However, the precise timing and extent to which oceanic anoxic conditions expanded during OAE 2  
32 remains unresolved. We present a new record of global ocean redox changes during OAE 2 using a  
33 combined geochemical and carbon cycle modelling approach. We utilize a continuous, high-resolution  
34 record of uranium isotopes in pelagic and platform-carbonate sediments to quantify the global extent  
35 of seafloor anoxia during OAE 2. This new dataset is then compared to a dynamic model of the coupled  
36 global carbon, phosphorus and uranium cycles to test hypotheses for OAE 2 initiation. This unique  
37 approach highlights an intra-OAE complexity that has previously been under constrained,  
38 characterized by two expansions of anoxia separated by an episode of globally significant  
39 reoxygenation coincident with the 'Plenus Cold Event'. Each anoxic expansion event was likely driven  
40 by rapid atmospheric CO<sub>2</sub> injections from multi-phase Large Igneous Province (LIP) activity.

41

42 **Significance Statement**

43 *Past ‘Oceanic Anoxic Events’ (OAEs) represent important carbon cycle perturbations that offer the*  
44 *opportunity to study the Earth’s response to extreme climate warming. A fundamental limitation for*  
45 *understanding OAEs is quantifying the timing and total extent of ocean anoxia. We present a*  
46 *quantitative account of global redox conditions for OAE 2 (~94 million years ago), using a high-*  
47 *resolution record of uranium isotopes combined with a biogeochemical model. We present new*  
48 *evidence for two discrete intervals of globally extensive anoxia that were coupled to enhanced*  
49 *terrestrial weathering, within the typically defined OAE interval. These anoxic intervals were separated*  
50 *by ocean reoxygenation and the temporary recovery of the carbon cycle.*

51

52 **Introduction**

53 Rapid climatic warming events have repeatedly punctuated Earth’s history and have often  
54 been associated with prolonged episodes of widespread oceanic anoxia. These intervals represent  
55 major disturbances to the global carbon cycle, which contributed to marine faunal turnover and mass  
56 extinctions (1). In particular, the Mesozoic Era was characterized by numerous prolonged intervals of  
57 globally enhanced anoxia, termed ‘Oceanic Anoxic Events’ (OAEs) (1). The Mesozoic OAEs are  
58 considered the model expression of oceanic anoxia in the Phanerozoic geological record, thus  
59 informing studies of past hyperthermal events and future environmental change (2, 3). Despite  
60 extensive study, the magnitude and timing of oceanic anoxia for OAEs are still poorly constrained,  
61 representing a fundamental limitation for defining these events. We address this shortcoming by  
62 presenting a new quantitative record of oceanic anoxia for OAE 2.

63 OAE 2 is the most widely recognised and severe OAE, occurring at the Cenomanian–Turonian  
64 Boundary (~94 Ma) (1) and lasting for up to ~900 thousand years (kyr) (4). A leading hypothesis for  
65 the initiation of OAE 2 is through the emplacement of one or more of the Caribbean, Madagascar and  
66 High-Arctic Large Igneous Provinces (LIPs) (1, 5-7) and an associated outgassing of CO<sub>2</sub> that caused  
67 climate warming and accelerated weathering (8). Such processes likely drove an increase in the supply  
68 of nutrients, especially phosphorus (P), to the ocean, and thereby increased productivity and oxygen  
69 demand through the aerobic degradation of organic matter (1, 5, 9). Productivity was potentially  
70 further amplified by the effective recycling of P from sediments overlain by anoxic waters (10-12).  
71 Ultimately, this chain of events led to anoxic water-column conditions and the enhanced preservation  
72 of organic carbon, which formed distinct black shales in marine sedimentary successions in many  
73 ocean basins. The preferential burial of isotopically light carbon (C) also contributed to a broad  
74 positive carbon-isotope excursion (CIE) across OAE 2 that is utilized as a global chemo-stratigraphic  
75 marker of the event (1). Silicate weathering and organic- carbon burial are vital components of the

76 global carbon cycle and represent important negative feedback mechanisms that sequester  
77 atmospheric CO<sub>2</sub> and drive climate stabilization during global warming events (8, 12, 13). However,  
78 the detailed behaviour of these recovery processes is currently limited for numerous carbon cycle  
79 perturbations in Earth history, including OAEs.

80 For OAE 2 there is widespread evidence of regionally extensive anoxia and euxinia (anoxic-  
81 sulfidic water-column conditions) in disparate localities, leading to benthic faunal extinctions, globally  
82 enhanced organic-carbon burial and the sequestration of redox-sensitive and chalcophilic trace metals  
83 (1, 9, 12, 14, 15). Oceanic anoxia is, however, a spatially heterogeneous condition, with a highly  
84 variable geochemical and sedimentary expression. A dependence on local redox indicators has  
85 significantly limited the integration of this important phenomenon into a global carbon cycle  
86 framework. To address this limitation, we present a quantitative record of the global extent of anoxia  
87 for OAE 2 using new, high-resolution uranium-isotope (<sup>238</sup>U/<sup>235</sup>U, reformulated as δ<sup>238</sup>U, see SI) data,  
88 in combination with a biogeochemical model that calculates changes in the coupled global C, P and U  
89 cycles. These new geochemical data come from well-preserved and extensively studied carbonate  
90 sediments that were deposited under oxygenated conditions in the European shelf sea and Tethyan  
91 continental margin during OAE 2. The studied sections (Fig. 1) include deeper shelf pelagic  
92 foraminiferal-nannofossil carbonates (chalks) from Eastbourne and South Ferriby (United Kingdom),  
93 and shallow-water platform carbonates from Raia del Pedale (Italy). We also present additional  
94 lithium-isotope data (<sup>7</sup>Li/<sup>6</sup>Li, reformulated as δ<sup>7</sup>Li (8)) for Eastbourne which supplement previously  
95 published results (8) to give a more highly resolved complementary record of changes in the global  
96 weathering regime during OAE 2.

97 Under anoxic conditions, oxidized and soluble U(VI) is drawn down from the water column  
98 and deposited in sediments as reduced and immobile U(IV), driving seawater U concentrations ([U])  
99 to lower values (16, 17). The primary isotopic fractionation of U is also strongly redox-dependent,  
100 whereby <sup>238</sup>U is preferentially sequestered in anoxic sediments, leaving the residual seawater  
101 relatively enriched in <sup>235</sup>U (18-25). This geochemical behaviour generates lower δ<sup>238</sup>U signatures in  
102 seawater that can be recorded in contemporary sediments. Moreover, because of the long residence  
103 time of U in the modern ocean (320–560 kyrs (16)) sedimentary δ<sup>238</sup>U signatures can resolve global  
104 changes in oceanic redox conditions (14, 26-29), which cannot be achieved by more traditional  
105 proxies.

106 For OAE 2, application of the U-isotope paleo-redox tracer is limited to a single study of  
107 organic-rich black shales (δ<sup>238</sup>U<sub>shale</sub>), wherein the data are suggestive of a three-fold increase in the  
108 extent of anoxia across the event (14). These data (Fig. 1) are of insufficient temporal resolution to  
109 provide insights into the rate and magnitude of ocean redox changes across the event or elucidate the

110 temporal relationship of ocean anoxia to other aspects of the Earth system response. Furthermore,  
111 the fractionation of U into black shales is strongly influenced by local geochemical controls (30) that  
112 complicate attempts to infer the 'global' U-isotope signature of oceanic redox changes. By contrast,  
113 the U-isotope signature of primary carbonate precipitates ( $\delta^{238}\text{U}_{\text{carb}}$ ) records the seawater isotopic  
114 composition ( $\delta^{238}\text{U}_{\text{sw}}$ ), with minimal additional fractionation under most environmental conditions  
115 (21, 25, 31, 32).

116 The new datasets presented here are used to test the current hypotheses for OAE 2 initiation,  
117 and the resulting biogeochemical changes, by acting as target outputs for the C–P–U model (see  
118 Methods and SI). This approach differs from other efforts to model U-isotope data in deep time (14,  
119 26-29), in that it calculates dynamic changes to the wider Earth system, including temperature,  
120 weathering, nutrient inputs, anoxia and carbon burial, driven by hypothesized perturbations to the  
121 carbon cycle. These changes, in turn, affect the oceanic U cycle. The benefit of this approach is that it  
122 gives an internally consistent, quantitative assessment of coupled changes in the carbon cycle.

123

## 124 **Results and Discussion**

125 **Geochemical Reconstruction of Oceanic Anoxia.** The stratigraphically expanded Eastbourne  
126 section has been extensively studied for a multitude of paleo-environmental proxies owing to its lack  
127 of significant diagenetic alteration (1, 8, 15, 33, 34) (see SI). In particular, the carbonates from  
128 Eastbourne have very low values of total organic carbon (TOC) (34) and were not subject to  
129 appreciable diagenetic sulfate reduction in pore waters (33), which should have minimized alteration  
130 of the primary  $\delta^{238}\text{U}_{\text{carb}}$  signatures. As such, the  $\delta^{238}\text{U}_{\text{carb}}$  record for Eastbourne should closely reflect  
131 variability in  $\delta^{238}\text{U}_{\text{sw}}$  throughout the OAE 2 interval and is hence used as the primary reference curve  
132 in the present study. The  $\delta^{238}\text{U}_{\text{carb}}$  record for Eastbourne has the highest resolution of the three sites  
133 and systematic temporal trends are statistically identified using a locally weighted polynomial  
134 smoothing function (LOESS) in order to prevent undue emphasis being placed on single data points.  
135 The South Ferriby section, although also showing a low degree of diagenetic alteration (see SI), is more  
136 lithified than Eastbourne, raising the possibility of greater secondary influences on  $\delta^{238}\text{U}_{\text{carb}}$ . It also  
137 contains a significant unconformity (Fig. 1) which is overlain by an organic-rich black shale.  
138 Mobilization of U from this horizon could potentially explain the comparatively high  $\delta^{238}\text{U}_{\text{carb}}$  values  
139 above the unconformity that are more typical of anoxic sediments (18, 19, 23, 30). Deposits at Raia  
140 del Pedale show evidence for partial recrystallization and dolomitization of originally mixed aragonite  
141 and high-magnesium-calcite producers (see SI). In particular the lowest  $\delta^{238}\text{U}_{\text{carb}}$  of the section are  
142 from dolomitized samples with anomalously high U/Ca (Fig. 1 and Fig. S3), consistent with the negative  
143  $\delta^{238}\text{U}_{\text{carb}}$  offset and U enrichment observed in modern dolomites (21, 31).

144 Multiple lines of evidence support the fidelity of the Eastbourne  $\delta^{238}\text{U}_{\text{carb}}$  record. First, despite  
145 potential diagenetic influences in the Raia del Pedale and South Ferriby sections, stability is seen in  
146 the  $\delta^{238}\text{U}_{\text{carb}}$  records post-dating OAE 2 at all three sites (Fig. 1). It is important to note that, during this  
147 stable post-OAE 2 interval,  $\delta^{238}\text{U}_{\text{shale}}$  values from the organic-rich black shales of Ocean Drilling  
148 Program (ODP) site 1261 (14) are  $\sim 0.5\text{‰}$  higher than contemporaneous  $\delta^{238}\text{U}_{\text{carb}}$  (Fig. 1). This offset is  
149 consistent with the observed magnitude and direction of U-isotope fractionation during U reduction  
150 in modern organic-rich sediments under an anoxic water column (18, 19, 23, 30) and therefore  
151 suggests that Eastbourne  $\delta^{238}\text{U}_{\text{carb}}$  closely reflects absolute values in  $\delta^{238}\text{U}_{\text{sw}}$ . Furthermore, during this  
152 stable period,  $\delta^{238}\text{U}_{\text{carb}}$  from Raia del Pedale and South Ferriby are  $\sim 0.2$  to  $0.3\text{‰}$  higher than  
153 Eastbourne which is consistent with observations from some modern bulk carbonate sediments that  
154 show higher  $\delta^{238}\text{U}_{\text{carb}}$  than seawater due to early diagenesis (31). These offsets, compared to  
155 Eastbourne, therefore likely reflect the diagenetic gradient between the carbonate sites and support  
156 a near-primary  $\delta^{238}\text{U}_{\text{sw}}$  signature at Eastbourne. In addition, there are two systematic decreases in  
157  $\delta^{238}\text{U}_{\text{carb}}$  at Eastbourne (Anoxia Expansion (AE) 1 and AE2, Fig. 2) which are associated with the  
158 progressive lowering of U/Ca and other redox-sensitive or chalcophilic trace metals ( $\text{TM}_{\text{redox}}$ ) at  
159 multiple localities, consistent with the removal of these elements into anoxic sediments. Finally, there  
160 is a broad coupling between two decreases in the  $\delta^{238}\text{U}_{\text{carb}}$  and  $\delta^7\text{Li}$  records (Fig. 2), which would not  
161 be preserved during diagenesis, and substantiates the veracity of both datasets.

162 At Eastbourne, the onset of the CIE, which typically defines the beginning of OAE 2, is closely  
163 associated with a systematic decrease in  $\delta^{238}\text{U}_{\text{carb}}$  from a maximum of  $-0.24 \pm 0.09\text{‰}$  (2SE) to a  
164 minimum of  $-0.71 \pm 0.06\text{‰}$  (AE1). This drop in values is accompanied by a decrease in  $\text{TM}_{\text{redox}}$  in  
165 multiple localities (35-37), including Eastbourne (Fig. 1 & 2) and Raia del Pedale (Fig. 1), suggesting the  
166 global expansion of oceanic anoxic conditions. After AE1,  $\delta^{238}\text{U}_{\text{carb}}$  rapidly increases to  $-0.41 \pm 0.07\text{‰}$   
167 suggesting a decrease in the extent of oceanic anoxia. This dramatic change directly corresponds to  
168 the onset of the Plenus Cold Event (PCE), an interval characterized by cooler temperatures at a range  
169 of latitudes (35, 38-45). Higher  $\delta^{238}\text{U}_{\text{carb}}$  values averaging  $-0.38 \pm 0.12 \text{‰}$  (1sd) were maintained  
170 throughout the PCE and correspond to widely observed  $\text{TM}_{\text{redox}}$  enrichments (35-37) (Fig. 1 & 2),  
171 indicating the decreased sequestration and oxidative liberation of these metals under more  
172 oxygenated conditions (35). The rise in  $\delta^{238}\text{U}_{\text{carb}}$  is also consistent with observations of local benthic  
173 faunal re-population and local reoxygenation in some basins, during the PCE (35, 36, 44-47).  
174 Importantly, the new  $\delta^{238}\text{U}_{\text{carb}}$  dataset indicates that the PCE reoxygenation was globally significant,  
175 returning the ocean to a redox state similar to pre-perturbation conditions.

176 The end of the PCE corresponds to a second systematic decrease in  $\delta^{238}\text{U}_{\text{carb}}$  (AE2). Again, the  
177 concentrations of  $\text{TM}_{\text{redox}}$  decrease at both Eastbourne (Fig. 2) and Raia del Pedale (35) indicating a

178 return to more expanded oceanic anoxia. Interestingly, the recovery of  $\delta^{238}\text{U}_{\text{carb}}$  from this decrease is  
179 poorly defined and appears more gradual, unlike the rapid changes in  $\delta^{238}\text{U}_{\text{carb}}$  observed for the PCE.  
180 The lack of a distinct post-OAE 2 recovery may indicate a lingering degree of anoxia after the CIE, or  
181 that insufficient time is recorded in these sections to observe the complete re-stabilization of the U  
182 and C cycles.

183 Both AE1 and AE2 are coupled to increased global temperatures, as indicated by  $\delta^{18}\text{O}$  in  
184 Eastbourne (Fig. 2) and organic geochemical proxies in North Atlantic sites (34, 42, 43, 45). Moreover,  
185 there is a coupled relationship between decreasing  $\delta^{238}\text{U}_{\text{carb}}$  and  $\delta^7\text{Li}$  during both AE1 and AE2 (Fig. 2),  
186 which is suggestive of a shift to a more congruent weathering regime (greater primary mineral  
187 dissolution than secondary mineral formation (8, 48) during these two anoxic intervals. These two  
188 intervals are also accompanied by independent evidence for an enhanced hydrological cycle (42),  
189 together suggesting two discrete periods of enhanced global weathering flux. In contrast to AE1 and  
190 AE2, the increasing  $\delta^{238}\text{U}_{\text{carb}}$  and reoxygenation during the PCE corresponds to cooler temperatures  
191 and drier conditions (34, 42, 45), as well as the recovery of  $\delta^7\text{Li}$  to more positive values. The coupling  
192 of datasets therefore empirically supports the hypothesized link between enhanced weathering  
193 activity under warmer climates, increased nutrient fluxes, heightened productivity and expanded  
194 oceanic anoxia (1, 8, 9, 42). Furthermore, the first interval of decreasing  $\delta^7\text{Li}$  and  $\delta^{238}\text{U}_{\text{carb}}$  (AE1) also  
195 temporally corresponds with a prominent decrease in osmium (Os) isotopes to more unradiogenic,  
196 basalt-like signatures that marks the main phase of LIP emplacement associated with the CIE (5-8).  
197 The return to more radiogenic Os-isotope signatures is not seen until after the PCE (5-7), reflecting a  
198 degree of continued volcanism across the cooling event, although two separate peaks in sedimentary  
199 Os concentrations may indicate multiple phases of heightened volcanic activity (5). LIP activity is  
200 therefore likely to have driven the two intervals of enhanced weathering activity and resulted in  
201 expanded oceanic anoxia.

202 **A biogeochemical model for OAE 2.** We use a C–P–U model (see SI) to examine if plausible  
203 fluxes of  $\text{CO}_2$  from LIP activity can indeed drive the magnitude of changes observed in  $\delta^{238}\text{U}_{\text{carb}}$ , U/Ca  
204 and  $\delta^{13}\text{C}$  at Eastbourne. The model is informed by previously established biogeochemical models (11,  
205 13, 49-52) and calculates the coupled dynamics of C, P and U cycling associated with changes in  
206 temperature, weathering and oceanic anoxia, in response to hypothesized  $\text{CO}_2$  perturbations. The C,  
207 P and U cycles are coupled together with the following processes (Fig. S2): (i) LIP  $\text{CO}_2$  emission, which  
208 acts as a source of C; (ii) seafloor spreading, which acts a source of C and a sink of U; (iii) silicate  
209 weathering, which is a sink of C and a source of P and U; (iv) primary production of organic matter,  
210 which is controlled by P availability and whose burial is a sink of C; (v) oxygen demand in the ocean,  
211 which is controlled by primary productivity and organic-matter remineralization rates, and determines

212 the extent of seafloor anoxia and the burial of U(IV) in anoxic sinks. The burial of organic C also results  
213 in an input of O<sub>2</sub> to the atmosphere. The U-isotope mass-balance is included in the model, allowing  
214 calculated  $\delta^{238}\text{U}_{\text{sw}}$  to trace the predicted extent of seafloor anoxia, whilst accounting for changes in U  
215 inputs linked to silicate weathering. Similarly,  $\delta^{13}\text{C}$  traces relative changes in the sources and sinks of  
216 inorganic and organic C.

217 The model is set up for mid-Cretaceous boundary conditions and the sensitivity to uncertainty  
218 in these parameters is discussed in the SI. Background atmospheric O<sub>2</sub> is a particularly important  
219 boundary condition. Varying O<sub>2</sub> in the model serves as a convenient way to account for uncertainty in  
220 the pre-existing degree of anoxia during the pre-OAE 2 interval, and hence the size of the ocean U  
221 reservoir (Fig. 3) and the sensitivity of the U cycle to CO<sub>2</sub> perturbations. Estimates of mid-Cretaceous  
222 atmospheric O<sub>2</sub> suggest greater than modern levels (49, 51, 53). Here, three baseline settings (O<sub>2</sub> =  
223 1.0, 1.1 and 1.2 times present atmospheric levels; PAL) are used to provide an envelope of uncertainty  
224 that reasonably captures pre-OAE 2 conditions, satisfies U cycle constraints, and covers the range of  
225 uncertainty in  $\delta^{238}\text{U}_{\text{carb}}$  (Fig. 2). The highest O<sub>2</sub> concentration setting (1.2 PAL) is the least sensitive to  
226 CO<sub>2</sub> perturbations and predicts modern levels of pre-OAE seafloor anoxia (0.3%) with the largest  
227 oceanic U reservoir (120% of today's size (16), and a higher baseline  $\delta^{238}\text{U}_{\text{sw}}$  of -0.30‰ (compared to  
228 modern seawater of  $-0.39 \pm 0.01\text{‰}$  (18, 21, 25, 30, 54).

229 **AE1.** Two CO<sub>2</sub> emission pulses were modelled, corresponding to AE1 and AE2, where the rate  
230 of CO<sub>2</sub> injection was kept constant for two discrete intervals of 150 kyrs. According to the C–P–U  
231 model, the  $\delta^{238}\text{U}_{\text{carb}}$  excursion during AE1 can be explained by a CO<sub>2</sub> degassing event of  $0.9\text{--}2.25 \times 10^{18}$   
232 mol C (i.e.  $0.6\text{--}1.5 \times 10^{13}$  mol C yr<sup>-1</sup>), which represents ~7 to 19% of current total degassing estimates  
233 for the combined Caribbean and Madagascar LIPs (see SI). This perturbation results in an increase of  
234 atmospheric CO<sub>2</sub> to 3.4–4.8 PAL (Fig. 3) and warming of 1.1–2.3°C, similar to independent proxy  
235 reconstructions (39, 41, 45). The resultant increase in silicate weathering drives a ~16–39% increase  
236 in P input ( $F_{\text{Pw}}$ ; Fig. S4), thereby increasing seawater P concentrations ([P]), promoting the expansion  
237 of anoxia and the sequestration of reduced U(IV), and preferentially <sup>238</sup>U, in anoxic sediments. The  
238 response of ocean nutrient levels, anoxia, and  $\delta^{238}\text{U}_{\text{sw}}$  are delayed compared to the CO<sub>2</sub> emission, with  
239 the maximum extent of seafloor anoxia occurring up to ~100 kyr after the end of the CO<sub>2</sub> injection,  
240 and covering between 8 and 15% of the total seafloor area (Fig. 3 and S4). This temporal lag is a  
241 function of the positive P feedback mechanism (see Fig. S4). When overlain by anoxic waters,  
242 sedimentary P burial efficiency is decreased (10, 11, 50, 51) due to i) the decreased flux of P absorbed  
243 to Fe-oxides ( $F_{\text{FeP}}$ ) and ii) an increased C/P of buried organic matter ( $(\text{C/P})_{\text{organic}}$ ), which suppresses  
244 productivity-driven increases in the burial of organic bound P ( $F_{\text{OrgP}}$ ). These processes inhibit seawater

245 P depletion in the model and fuel further productivity even when external nutrient inputs are  
246 declining, a result which is consistent with published sedimentary P data for OAE 2 (12).

247 **PCE.** Carbon sequestration from silicate weathering and the burial of marine-derived organic  
248 matter increase during AE1 by 16–30% and 20–33% respectively, compared with pre-OAE 2 conditions  
249 (Fig. S4). These processes drive the decrease of atmospheric CO<sub>2</sub> after the LIP emission ended,  
250 resulting in a temperature and weathering decrease, and hence also a decrease in F<sub>Pw</sub> (Fig. S4). The  
251 combination of decreased F<sub>Pw</sub>, continued high Ca-bound P burial (F<sub>CaP</sub>) and high F<sub>OrgP</sub> burial, leads to a  
252 [P] decrease (Fig. S4), and hence biological productivity also decreases. The burial of organic matter  
253 under anoxic conditions further drives a minor (~0.02 PAL) net increase in atmospheric O<sub>2</sub> during AE1  
254 (Fig. S4). As a result of these controls, ocean oxygenation progresses and is positively re-enforced by  
255 the enhanced P removal from increased F<sub>FeP</sub> burial and decreased (C/P)<sub>organic</sub> (Fig. S4). In response,  
256  $\delta^{238}\text{U}_{\text{sw}}$  recovers relatively quickly as oceanic anoxia declines, due to the depleted global U reservoir,  
257 whilst [U] recovers more slowly, reaching maximum values up to 100 kyrs later (Fig. 3). This process  
258 could explain the stratigraphic lag between increasing  $\delta^{238}\text{U}_{\text{carb}}$  and U/Ca during the PCE (Fig. 1 and 2;  
259 see the below discussion). During the onset of oxygenation and increase in  $\delta^{238}\text{U}_{\text{sw}}$ ,  $\delta^{13}\text{C}$  also continues  
260 to rise owing to the slower dynamics of the larger C reservoir, again consistent with the trends shown  
261 at Eastbourne for the start of the PCE (Fig. 2). Eventually, the decreased burial of organic matter, and  
262 thus isotopically light carbon, during the reoxygenation episode begins to generate the carbon-isotope  
263 ‘trough’ that is used for the chemo-stratigraphic correlation of the PCE (35, 45, 55, 56).

264 Despite the  $\delta^{238}\text{U}_{\text{carb}}$  increase during the PCE being consistent with the observations of cooler  
265 conditions and local benthic reoxygenation (35, 36, 44-47, 57), the magnitude and abrupt rise of the  
266  $\delta^{238}\text{U}_{\text{carb}}$  at Eastbourne is difficult to simulate with the C–P–U model, assuming that this feature is not  
267 an artifact of a condensed sedimentary interval. Indeed, the modelled  $\delta^{238}\text{U}_{\text{sw}}$  recovery better  
268 corresponds to the later phase of the PCE, when TM<sub>redox</sub> also recover. The rapidity of the  $\delta^{238}\text{U}_{\text{carb}}$   
269 increase, and delay of the TM<sub>redox</sub> enrichments, implies a greater sensitivity of  $\delta^{238}\text{U}_{\text{carb}}$  to changing  
270 redox conditions, compared to trace-metal concentrations. Such sensitivity was likely driven by an  
271 additional decrease in the dynamic residence time of U, already greatly reduced to a minimum of ~45  
272 kyrs (O<sub>2</sub> = 1 scenario) during AE1, due to the burial of U(IV) in anoxic sinks. This reduction might have  
273 been accomplished by further U drawdown in the ‘hypoxic’ U sink (i.e. sediments that are reducing at  
274 depth, beneath a fully, or poorly oxygenated water column (19)), which is not accounted for in the  
275 model, and would have had little impact on  $\delta^{238}\text{U}_{\text{carb}}$ . Under such conditions  $\delta^{238}\text{U}_{\text{carb}}$  would more  
276 precisely capture the onset of reoxygenation than TM<sub>redox</sub>. Alternatively, this model–data discrepancy  
277 may be explained by the oxidation and loss of U from shales previously deposited under anoxic  
278 conditions, as has been observed in modern continental-margin sediments (58), and is similar to the

279 mechanism proposed to explain transiently light  $\delta^{34}\text{S}_{\text{CAS}}$  values during the PCE (15, 35). This additional  
280 supply of isotopically heavy U to the ocean would act to amplify the  $\delta^{238}\text{U}_{\text{sw}}$  increase due to the  
281 decrease in anoxic sinks, and could further explain the faster response compared to  $\text{TM}_{\text{redox}}$ . It is also  
282 plausible that reoxygenation could have been accelerated by mechanisms not considered in our  
283 model, such as sea level or temperature changes (9, 59), or the additional supply of  $\text{O}_2$  caused by pyrite  
284 burial (49, 53).

285 **AE2.** An assumed second  $\text{CO}_2$  injection, of lesser magnitude ( $0.4\text{--}1.05 \times 10^{13} \text{ molC yr}^{-1}$ ) but of  
286 the same duration as the first event, generates a return to warmer conditions after the PCE. This  
287 increase in temperature results in a return of widespread anoxia and a smaller negative shift in  $\delta^{238}\text{U}_{\text{sw}}$   
288 by  $-0.2\%$ , equivalent to an expansion of oceanic anoxia of 3–8% of the total seafloor area. This  
289 modelled  $\text{CO}_2$  injection also results in the addition of isotopically light carbon to the ocean-  
290 atmosphere system that augments the decrease in  $^{12}\text{C}$ -enriched carbon burial during the PCE  
291 reoxygenation episode, thereby accelerating the development of the  $\delta^{13}\text{C}$  ‘trough’ of the PCE. Despite  
292 this minor negative excursion, relatively elevated  $\delta^{13}\text{C}$  values occur throughout the entire OAE 2  
293 interval owing to the slower dynamics of the relatively large carbon reservoir.

294 **Wider Implications for OAEs.** Characterizing the timing, duration and extent of oceanic anoxia  
295 during OAE 2 is fundamental to understanding the driving mechanisms of these extreme perturbations  
296 to the carbon cycle and climate system. In an attempt to replicate the distribution of anoxia indicated  
297 by local redox proxies, Earth System modelling suggests 50% of the global ocean volume was dysoxic  
298 or anoxic (9) whilst the shale-derived  $\delta^{238}\text{U}$  estimate suggests only 1–2% of the seafloor was overlain  
299 by anoxic waters (14). By contrast, the new carbonate-derived  $\delta^{238}\text{U}$  dataset presented here provides  
300 a better systematic resolution of the timing and magnitude of ocean deoxygenation (Fig. 1), suggesting  
301 that between 8% and 15% of the seafloor was overlain by an anoxic water column. This reconstruction  
302 is in close agreement with recent estimates from thallium isotopes (60) and is compatible with 2–5%  
303 of seafloor being euxinic, based on modelling of the sulfur- and molybdenum-isotope systems (15, 46,  
304 61), as this extreme chemical state would only make up a fraction of the total anoxic ocean, and  $\delta^{238}\text{U}$   
305 does not discriminate between anoxic and euxinic redox states. The importance of differentiating  
306 these two redox states is increasingly being recognized for periods of expanded anoxia (e.g. 62).  
307 Crucially, the high resolution of the  $\delta^{238}\text{U}_{\text{carb}}$  data uniquely resolves at least two fluctuations between  
308 episodes of globally expanded and contracted anoxia during the traditionally defined OAE 2 interval.  
309 Such findings are likely applicable for other OAEs where there are suggestions of local redox and  
310 temperature variability, such as the Aptian OAE 1a (1).

311 The C–P–U model successfully generates the magnitude of U-isotope excursions through fairly  
312 conservative  $\text{CO}_2$  degassing levels and subsequent changes in global temperature. These amounts of

313 CO<sub>2</sub> degassing probably represent upper estimates since the model does not consider many  
314 contributory deoxygenation mechanisms, including the inverse relationship between temperature  
315 and O<sub>2</sub> solubility, or changes in O<sub>2</sub> supply through variable ocean ventilation rates (9). We suggest that  
316 these additional mechanisms are of second-order importance to changes in terrestrial weathering for  
317 driving OAE 2, although they could help refine our understanding of the precise temporal and  
318 geographical distribution of oceanic redox changes.

319 In summary, the coupled geochemical and modelling approach adopted here for OAE 2 allows  
320 for an internally consistent examination of global-scale deoxygenation during carbon cycle  
321 perturbation events. The new U-isotope dataset highlights globally significant oscillations in oceanic  
322 redox conditions within the traditionally defined OAE 2 interval that are closely coupled to changes in  
323 global temperature and hydrological regime. The C–P–U model successfully reproduces the trends in  
324  $\delta^{238}\text{U}_{\text{carb}}$  through discrete atmospheric CO<sub>2</sub> injections, suggesting that the exceptional longevity of OAE  
325 2 was the result of multi-phase LIP activity.

326

## 327 **Materials and Methods**

328 **Uranium-isotope analysis.** Carbonate samples were mechanically cleaned for weathered  
329 surfaces. Sample powders underwent oxidative-reductive cleaning (63, 64), before selective digestion  
330 using 1 M buffered sodium acetate. U-isotope composition was determined using a <sup>236</sup>U-<sup>233</sup>U double  
331 spike to correct for instrumental mass fractionation, where uranium was pre-concentrated by co-  
332 precipitation and purified by ion-exchange chromatographic procedures using a single column packed  
333 with UTEVA resin (Eichrom Technologies, USA) (20, 21, 23, 65, 66). Uranium-isotope measurements  
334 were performed by multiple-collector inductively coupled plasma mass spectrometer (MC-ICP-MS) at  
335 the Centre for Trace Element Analysis, University of Otago, New Zealand (19, 21-23). **Lithium-isotope**  
336 **methods.** An additional 8 samples were analyzed from the Eastbourne section for Li isotopes, to  
337 increase the resolution of the already existing dataset, following the same original protocols (8).  
338 Carbonate samples were leached using 0.1 M HCl for 1 hr and sample solutions were purified using a  
339 two-stage cation-exchange procedure. Analyses were performed by MC-ICP-MS at Oxford University,  
340 U.K. (8). **Coupled C–P–U model.** The box-model is a simplified version of elements of the Geochemical  
341 Carbon cycle model (GEOCARB) and the Carbon, Oxygen, Phosphorus, Sulphur and Evolution (COPSE)  
342 Earth System model (11, 13, 49-52), focusing exclusively on the shorter term processes of the carbon  
343 and phosphorus cycles. The model incorporates U reservoirs and the isotopic mass-balance equations  
344 for C and U isotopes as tracers of the predicted outcomes to assumed CO<sub>2</sub> emission perturbations.

345

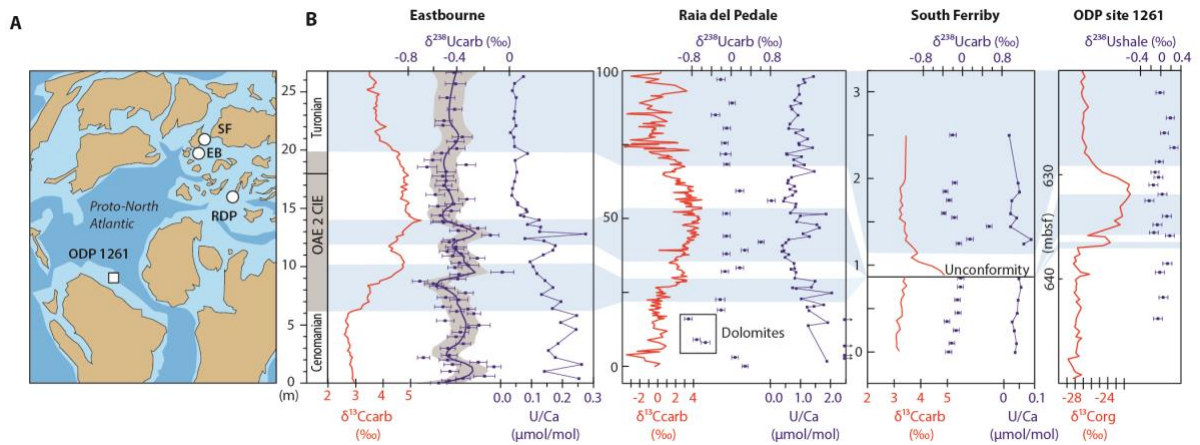
## 346 **Acknowledgments**

347 We thank the anonymous reviewers of this work for their constructive inputs. We thank Malcolm Reid  
348 and David Barr for laboratory support. For their contributions to this work MOC, CHS, CMM, IRC and  
349 HCJ were supported by the Marsden Fund Council from government funding, managed by the Royal  
350 Society of New Zealand (UOO1314). T.M.L. was supported by the Natural Environment Research  
351 Council "Jurassic Earth System and Timescale" large grant and a Royal Society Wolfson Research Merit  
352 Award. P.A.E.P.v.S. was funded by European Research Council Consolidator Grant 682760  
353 CONTROLPASTCO2.

354

355

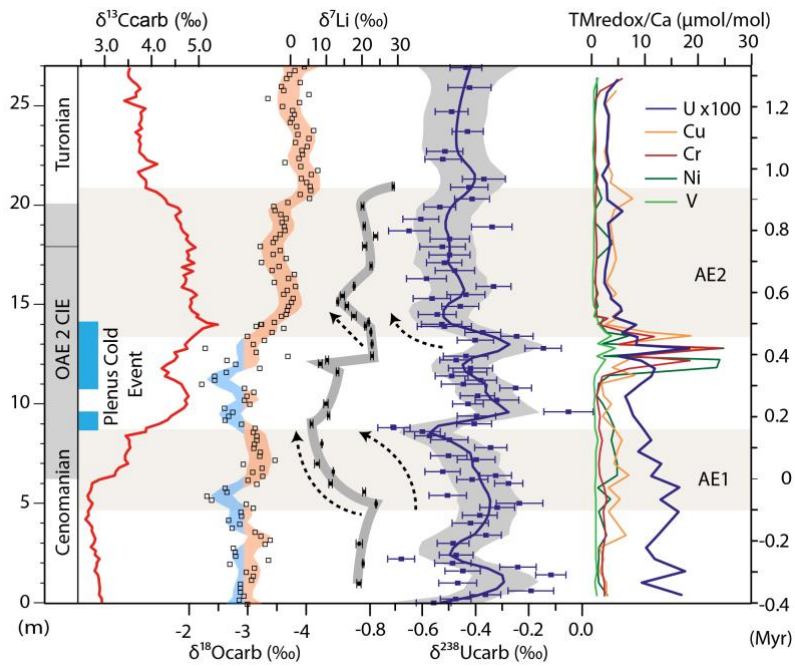
356



357

358 **Fig. 1:** A. Paleogeographic reconstruction showing locations of Eastbourne (EB),  
359 Raia del Pedale (RDP),  
360 South Ferriby (SF) and ODP site 1261, modified with permission from (67) B.  $\delta^{13}\text{C}$  (15, 34, 68),  $\delta^{238}\text{U}_{\text{carb}}$   
361 ( $\pm 2\text{SE}$ ) and U/Ca (35 and this study) for EB, RDP and SF in comparison to  $\delta^{13}\text{C}_{\text{Org}}$  and  $\delta^{238}\text{U}$  from black  
shales at ODP site 1261 (14, 55). Correlations (blue shading) are from previous work (8, 15, 35).

362

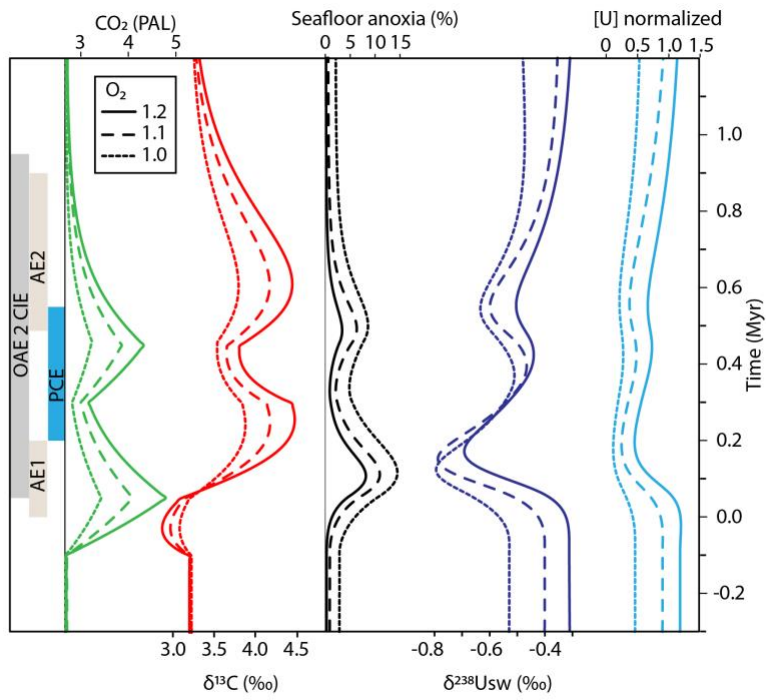


364

365 **Fig. 2:** Complementary geochemical datasets ( $\delta^{13}\text{C}$ ,  $\delta^{18}\text{O}$  and  $\delta^7\text{Li}$ ) (8, 34), together with the  $\delta^{238}\text{U}_{\text{carb}}$   
 366 and  $\text{TM}_{\text{redox}}$  datasets for Eastbourne (35). ‘Anoxic Expansion’ episodes (AE1 and AE2) are identified  
 367 from coupled negative  $\delta^{238}\text{U}_{\text{carb}}$  excursions and  $\text{TM}_{\text{redox}}$  decreases. Unusual boreal faunas (blue bar)  
 368 and less negative  $\delta^{18}\text{O}$  are indicative of cooler waters and mark the ‘Plenus Cold Event’ (PCE) (35, 38,  
 369 56). Black dashed arrows indicate periods of broad coupling between  $\delta^7\text{Li}$  and  $\delta^{238}\text{U}_{\text{carb}}$ . The positive  
 370  $\delta^{13}\text{C}$  excursion (34) is traditionally used to define OAE 2 (grey shading). Timescale (right axis) is based  
 371 on estimates for OAE 2 of up to  $\sim 900$  kyrs (4) and a linear age model, with 0 kyrs marking the start of  
 372 the CIE.

373

374



375

376

377 **Fig 3:** C–P–U model outputs in relation to events of OAE 2 identified in the  $\delta^{238}\text{U}_{\text{carb}}$  dataset of this

378 study (upper panel). Time (vertical axis) is given relative to the approximate start of the CIE, as in Fig.

379 2.

380

381 **References**

- 382 1. Jenkyns HC (2010) Geochemistry of oceanic anoxic events. *Geochemistry Geophysics*  
383 *Geosystems*. 11 Q03004, doi:10.1029/2009gc002788.
- 384 2. Watson AJ, Lenton TM, & Mills BJW (2017) Ocean deoxygenation, the global phosphorus  
385 cycle and the possibility of human-caused large-scale ocean anoxia. *Philosophical*  
386 *Transactions of the Royal Society A: Mathematical, Physical and Engineering Sciences* 375A.
- 387 3. Dickson AJ, *et al.* (2014) The spread of marine anoxia on the northern Tethys margin during  
388 the Paleocene - Eocene Thermal Maximum. *Paleoceanography* 29(6):471-488.
- 389 4. Eldrett JS, *et al.* (2015) An astronomically calibrated stratigraphy of the Cenomanian,  
390 Turonian and earliest Coniacian from the Cretaceous Western Interior Seaway, USA:  
391 Implications for global chronostratigraphy. *Cretaceous Research* 56:316–344.
- 392 5. Turgeon SC & Creaser RA (2008) Cretaceous Oceanic Anoxic Event 2 triggered by a massive  
393 magmatic episode. *Nature* 454(7202):323–326.
- 394 6. Du Vivier AD, *et al.* (2014) Marine <sup>187</sup>Os/<sup>188</sup>Os isotope stratigraphy reveals the interaction of  
395 volcanism and ocean circulation during Oceanic Anoxic Event 2. *Earth and Planetary Science*  
396 *Letters* 389:23–33.
- 397 7. Du Vivier A, Selby D, Condon D, Takashima R, & Nishi H (2015) Pacific <sup>187</sup>Os/<sup>188</sup>Os isotope  
398 chemistry and U–Pb geochronology: Synchronicity of global Os isotope change across OAE 2.  
399 *Earth and Planetary Science Letters* 428:204-216.
- 400 8. Pogge von Strandmann PAE, Jenkyns HC, & Woodfine RG (2013) Lithium isotope evidence  
401 for enhanced weathering during Oceanic Anoxic Event 2. *Nat. Geosci.* 6(8):668–672.
- 402 9. Monteiro F, Pancost R, Ridgwell A, & Donnadieu Y (2012) Nutrients as the dominant control  
403 on the spread of anoxia and euxinia across the Cenomanian-Turonian oceanic anoxic event  
404 (OAE 2): Model - data comparison. *Paleoceanography*. 27:(4).PA4209,  
405 doi:10.1029/2012PA002351.
- 406 10. Van Cappellen P & Ingall ED (1994) Benthic phosphorus regeneration, net primary  
407 production, and ocean anoxia - a model of the coupled marine biogeochemical cycles of  
408 carbon and phosphorus. *Paleoceanography* 9(5):677-692.
- 409 11. Handoh IC & Lenton TM (2003) Periodic mid-Cretaceous Oceanic Anoxic Events linked by  
410 oscillations of the phosphorus and oxygen biogeochemical cycles. *Global Biogeochemical*  
411 *Cycles* 17(4).
- 412 12. Mort HP, *et al.* (2007) Phosphorus and the roles of productivity and nutrient recycling during  
413 Oceanic Anoxic Event 2. *Geology* 35(6):483–486.

- 414 13. Berner RA & Kothavala Z (2001) GEOCARB III: A revised model of atmospheric CO<sub>2</sub> over  
415 Phanerozoic time. *American Journal of Science* 301(2):182–204.
- 416 14. Montoya-Pino C, *et al.* (2010) Global enhancement of ocean anoxia during Oceanic Anoxic  
417 Event 2: A quantitative approach using U isotopes. *Geology* 38(4):315–318.
- 418 15. Owens JD, *et al.* (2013) Sulfur isotopes track the global extent and dynamics of euxinia  
419 during Cretaceous Oceanic Anoxic Event 2. *Proceedings of the National Academy of Sciences*  
420 *of the United States of America* 110(46):18407–18412.
- 421 16. Dunk R, Mills R, & Jenkins W (2002) A reevaluation of the oceanic uranium budget for the  
422 Holocene. *Chem. Geol.* 190(1):45–67.
- 423 17. Anderson R (1987) Redox behavior of uranium in an anoxic marine basin. *Uranium* 3(2-  
424 4):145–164.
- 425 18. Andersen MB, *et al.* (2016) Closing in on the marine <sup>238</sup>U/<sup>235</sup>U budget. *Chem. Geol.* 420:11–  
426 22.
- 427 19. Andersen MB, Stirling CH, & Weyer S (2017) Uranium isotope fractionation. *Rev. Mineral.*  
428 *Geochem* 82(1):799–850.
- 429 20. Stirling CH, Andersen MB, Warthmann R, & Halliday AN (2015) Isotope fractionation of <sup>238</sup>U  
430 and <sup>235</sup>U during biologically-mediated uranium reduction. *Geochimica et Cosmochimica Acta*  
431 163:200–218.
- 432 21. Stirling CH, Andersen MB, Potter E-K, & Halliday AN (2007) Low-temperature isotopic  
433 fractionation of uranium. *Earth and Planetary Science Letters* 264(1):208–225.
- 434 22. Hinojosa JL, Stirling CH, Reid MR, Moy CM, & Wilson GS (2016) Trace metal cycling and  
435 <sup>238</sup>U/<sup>235</sup>U in New Zealand’s fjords: Implications for reconstructing global paleoredox  
436 conditions in organic-rich sediments. *Geochimica et Cosmochimica Acta* 179:89–109.
- 437 23. Rolison JM, C.H.Stirling, Middag R, & Rijkenberg MJA (2017) Uranium stable isotope  
438 fractionation in the Black Sea: Modern calibration of the <sup>238</sup>U/<sup>235</sup>U paleoredox proxy. .  
439 *Geochimica et Cosmochimica Acta* 203:69–88.
- 440 24. Noordmann J, *et al.* (2015) Uranium and molybdenum isotope systematics in modern euxinic  
441 basins: Case studies from the central Baltic Sea and the Kyllaren fjord (Norway). *Chem. Geol.*  
442 396:182–195.
- 443 25. Weyer S, *et al.* (2008) Natural fractionation of <sup>238</sup>U/<sup>235</sup>U. *Geochimica et Cosmochimica Acta*  
444 72(2):345-359.
- 445 26. Brenneka GA, Herrmann AD, Algeo TJ, & Anbar AD (2011) Rapid expansion of oceanic  
446 anoxia immediately before the end-Permian mass extinction. *Proceedings of the National*  
447 *Academy of Sciences of the United States of America* 108(43):17631–17634.

- 448 27. Dahl TW, *et al.* (2014) Uranium isotopes distinguish two geochemically distinct stages during  
449 the later Cambrian SPICE event. *Earth and planetary science letters* 401:313–326.
- 450 28. Lau KV, *et al.* (2016) Marine anoxia and delayed Earth system recovery after the end-  
451 Permian extinction. *Proceedings of the National Academy of Sciences* 113(9):2360–2365.
- 452 29. Elrick M, *et al.* (2017) Global-ocean redox variation during the middle-late Permian through  
453 Early Triassic based on uranium isotope and Th/U trends of marine carbonates. *Geology*  
454 45(2):163-166.
- 455 30. Andersen M, *et al.* (2014) A modern framework for the interpretation of  $^{238}\text{U}/^{235}\text{U}$  in studies  
456 of ancient ocean redox. *Earth and Planetary Science Letters* 400:184–194.
- 457 31. Romaniello SJ, Herrmann AD, & Anbar AD (2013) Uranium concentrations and  $^{238}\text{U}/^{235}\text{U}$   
458 isotope ratios in modern carbonates from the Bahamas: Assessing a novel paleoredox proxy.  
459 *Chem. Geol.* 362:305–316.
- 460 32. Chen X, Romaniello SJ, Herrmann AD, Wasylenki LE, & Anbar AD (2016) Uranium isotope  
461 fractionation during coprecipitation with aragonite and calcite. *Geochimica et Cosmochimica*  
462 *Acta* 188:189–207.
- 463 33. Owens JD, *et al.* (2012) Iron isotope and trace metal records of iron cycling in the proto -  
464 North Atlantic during the Cenomanian - Turonian oceanic anoxic event (OAE 2).  
465 *Paleoceanography*. 27.PA3223, doi:10.1029/2012PA002328.
- 466 34. Tsikos H, *et al.* (2004) Carbon-isotope stratigraphy recorded by the Cenomanian–Turonian  
467 Oceanic Anoxic Event: correlation and implications based on three key localities. *J. Geol. Soc.*  
468 161(4):711–719.
- 469 35. Jenkyns HC, Dickson AJ, Ruhl M, & Van den Boorn SHJM (2017) Basalt–seawater interaction,  
470 the Plenus Cold Event, enhanced weathering, and geochemical change: deconstructing OAE  
471 2 (Cenomanian–Turonian, Late Cretaceous). *Sedimentology* 64:16–43.
- 472 36. Eldrett JS, Minisini D, & Bergman SC (2014) Decoupling of the carbon cycle during Ocean  
473 Anoxic Event 2. *Geology* 42(7):567–570.
- 474 37. Snow LJ, Duncan RA, & Bralower TJ (2005) Trace element abundances in the Rock Canyon  
475 Anticline, Pueblo, Colorado, marine sedimentary section and their relationship to Caribbean  
476 plateau construction and Ocean Anoxic Event 2. *Paleoceanography*.  
477 20.doi:10.1029/2004PA001093.
- 478 38. Gale AS & Christensen WK (1996) Occurrence of the belemnite *Actinocamax plenus* in the  
479 Cenomanian of SE France and its significance. *Bulletin of the Geological Society of Denmark*  
480 43:68–77.

- 481 39. Voigt S, Gale AS, & Flögel S (2004) Midlatitude shelf seas in the Cenomanian - Turonian  
482 greenhouse world: Temperature evolution and North Atlantic circulation.  
483 *Paleoceanography*. 19.PA4020, doi:10.1029/2004PA001015.
- 484 40. Voigt S, Gale AS, & Voigt T (2006) Sea-level change, carbon cycling and palaeoclimate during  
485 the Late Cenomanian of northwest Europe; an integrated palaeoenvironmental analysis.  
486 *Cretaceous Research* 27(6):836-858.
- 487 41. Voigt S, Wilmsen M, Mortimore R, & Voigt T (2003) Cenomanian palaeotemperatures  
488 derived from the oxygen isotopic composition of brachiopods and belemnites: evaluation of  
489 Cretaceous palaeotemperature proxies. *International Journal of Earth Sciences* 92(2):285-  
490 299.
- 491 42. van Helmond NA, *et al.* (2014) A perturbed hydrological cycle during Oceanic Anoxic Event 2.  
492 *Geology* 42(2):123-126.
- 493 43. Sinninghe Damsté JS, van Bentum EC, Reichart G-J, Pross J, & Schouten S (2010) A CO<sub>2</sub>  
494 decrease-driven cooling and increased latitudinal temperature gradient during the mid-  
495 Cretaceous Oceanic Anoxic Event 2. *Earth and Planetary Science Letters* 293(1):97–103.
- 496 44. Jarvis I, Lignum JS, Gröcke DR, Jenkyns HC, & Pearce MA (2011) Black shale deposition,  
497 atmospheric CO<sub>2</sub> drawdown, and cooling during the Cenomanian–Turonian Oceanic Anoxic  
498 Event. *Paleoceanography*. 26:(3).PA3201, doi:10.1029/2010PA002081.
- 499 45. Forster A, Schouten S, Moriya K, Wilson PA, & Sinninghe Damsté JS (2007) Tropical warming  
500 and intermittent cooling during the Cenomanian/Turonian Oceanic Anoxic Event 2: Sea  
501 surface temperature records from the equatorial Atlantic. *Paleoceanography*. 22.PA1219,  
502 doi:10.1029/2006PA001349.
- 503 46. Dickson AJ, Jenkyns HC, Porcelli D, van den Boorn S, & Idiz E (2016) Basin-scale controls on  
504 the molybdenum-isotope composition of seawater during Oceanic Anoxic Event 2 (Late  
505 Cretaceous). *Geochimica et Cosmochimica Acta* 178:291–306.
- 506 47. Kuhnt W, Luderer F, Nederbragt S, Thurow J, & Wagner T (2005) Orbital-scale record of the  
507 late Cenomanian–Turonian oceanic anoxic event (OAE 2) in the Tarfaya Basin (Morocco).  
508 *International Journal of Earth Sciences* 94(1):147–159.
- 509 48. Pogge von Strandmann PAE & Henderson GM (2015) The Li isotope response to mountain  
510 uplift. *Geology* 43(1):67–70.
- 511 49. Bergman JM, Lenton TM, & Watson AJ (2004) COPSE: A new model of biogeochemical  
512 cycling over Phanerozoic time. *American Journal of Science* 304(397).
- 513 50. Lenton TM & Watson AJ (2000) Redfield revisited: 1. Regulation of nitrate, phosphate, and  
514 oxygen in the ocean. *Global Biogeochemical Cycles* 14(1):225–248.

- 515 51. Lenton TM & Watson AJ (2000) Redfield revisited: 2. What regulates the oxygen content of  
516 the atmosphere? *Global Biogeochemical Cycles* 14(1):249–268.
- 517 52. Slomp CP & Van Cappellen P (2007) The global marine phosphorus cycle: sensitivity to  
518 oceanic circulation. *Biogeosciences* 4(2):155–171.
- 519 53. Mills BJ, Belcher CM, Lenton TM, & Newton RJ (2016) A modeling case for high atmospheric  
520 oxygen concentrations during the Mesozoic and Cenozoic. *Geology* 44(12):1023–1026.
- 521 54. Tissot FL & Dauphas N (2015) Uranium isotopic compositions of the crust and ocean: age  
522 corrections, U budget and global extent of modern anoxia. *Geochimica et Cosmochimica*  
523 *Acta* 167:113–143.
- 524 55. Erbacher J, Friedrich O, Wilson PA, Birch H, & Mutterlose J (2005) Stable organic carbon  
525 isotope stratigraphy across Oceanic Anoxic Event 2 of Demerara Rise, western tropical  
526 Atlantic. *Geochemistry, Geophysics, Geosystems*. 6.doi:10.1029/2004GC000850.
- 527 56. Gale A, Jenkyns H, Kennedy W, & Corfield R (1993) Chemostratigraphy versus  
528 biostratigraphy: data from around the Cenomanian–Turonian boundary. *J. Geol. Soc.*  
529 150:29–32.
- 530 57. Friedrich O (2010) Benthic foraminifera and their role to decipher paleoenvironment during  
531 mid-Cretaceous Oceanic Anoxic Events—the “anoxic benthic foraminifera” paradox. *Revue de*  
532 *micropaléontologie* 53(3):175–192.
- 533 58. Morford JL, Martin WR, & Carney CM (2009) Uranium diagenesis in sediments underlying  
534 bottom waters with high oxygen content. *Geochimica et Cosmochimica Acta* 73(10):2920–  
535 2937.
- 536 59. Ozaki K & Tajika E (2013) Biogeochemical effects of atmospheric oxygen concentration,  
537 phosphorus weathering, and sea-level stand on oceanic redox chemistry: Implications for  
538 greenhouse climates. *Earth and Planetary Science Letters* 373:129–139.
- 539 60. Ostrander CM, Owens JD, & Nielsen SG (2017) Constraining the rate of oceanic  
540 deoxygenation leading up to a Cretaceous Oceanic Anoxic Event (OAE-2:~ 94 Ma). *Science*  
541 *Advances* 3(8):e1701020.
- 542 61. Dickson AJ, *et al.* (2016) Corrigendum to " Basin-scale controls on the molybdenum-isotope  
543 composition of seawater during Oceanic Anoxic Event 2 (Late Cretaceous)"[*Geochim.*  
544 *Cosmochim. Acta* 178 (2016) 291-306]. *Geochimica et Cosmochimica Acta* 189:404–405.
- 545 62. Poulton SW & Canfield DE (2011) Ferruginous Conditions: A Dominant Feature of the Ocean  
546 through Earth's History. *Elements* 7(2):107-112.
- 547 63. Bian N & Martin PA (2010) Investigating the fidelity of Mg/Ca and other elemental data from  
548 reductively cleaned planktonic foraminifera. *Paleoceanography* 25.

- 549 64. Boyle E & Rosenthal Y (1996) Chemical hydrography of the South Atlantic during the last  
550 glacial maximum: Cd vs.  $\delta^{13}\text{C}$ . *The South Atlantic*, (Springer), pp 423-443.
- 551 65. Amelin Y, *et al.* (2010) U–Pb chronology of the Solar System's oldest solids with variable  $^{238}$   
552  $\text{U}/^{235}\text{U}$ . *Earth and Planetary Science Letters* 300(3):343–350.
- 553 66. Murphy MJ, Stirling CH, Kaltenbach A, Turner SP, & Schaefer BF (2014) Fractionation of  
554  $^{238}\text{U}/^{235}\text{U}$  by reduction during low temperature uranium mineralisation processes. *Earth and*  
555 *Planetary Science Letters* 388:306–317.
- 556 67. Zhou X, *et al.* (2015) Upper ocean oxygenation dynamics from I/Ca ratios during the  
557 Cenomanian–Turonian OAE 2. *Paleoceanography* 30:510-526.
- 558 68. Jenkyns HC, Matthews A, Tsikos H, & Erel Y (2007) Nitrate reduction, sulfate reduction, and  
559 sedimentary iron isotope evolution during the Cenomanian - Turonian oceanic anoxic event.  
560 *Paleoceanography*. 22.PA3208, doi:10.1029/2006PA001355.
- 561 69. Andersen MB, *et al.* (2015) The terrestrial uranium isotope cycle. *Nature* 517(7534):356–  
562 359.
- 563 70. Tessier A, Campbell PG, & Bisson M (1979) Sequential extraction procedure for the  
564 speciation of particulate trace metals. *Anal. Chem.* 51(7):844–851.
- 565 71. Canfield DE (1998) A new model for Proterozoic ocean chemistry. *Nature* 396(6710):450–  
566 453.
- 567 72. Lenton TM & Daines SJ (2017) Biogeochemical transformations in the history of the ocean.  
568 *Annual Review of Marine Science* 9:31–58.
- 569 73. Helly JJ & Levin LA (2004) Global distribution of naturally occurring marine hypoxia on  
570 continental margins. *Deep Sea Research Part I: Oceanographic Research Papers* 51(9):1159–  
571 1168.
- 572 74. Jones CE & Jenkyns HC (2001) Seawater strontium isotopes, oceanic anoxic events, and  
573 seafloor hydrothermal activity in the Jurassic and Cretaceous. *American Journal of Science*  
574 301(2):112–149.
- 575 75. Mills B, Daines SJ, & Lenton TM (2014) Changing tectonic controls on the long - term carbon  
576 cycle from Mesozoic to present. *Geochemistry, Geophysics, Geosystems* 15(12):4866–4884.
- 577 76. Holmden C, Amini M, & Francois R (2015) Uranium isotope fractionation in Saanich Inlet: A  
578 modern analog study of a paleoredox tracer. *Geochimica et Cosmochimica Acta* 153:202–  
579 215.
- 580 77. Noordmann J, Weyer S, Georg RB, Jöns S, & Sharma M (2015)  $^{238}\text{U}/^{235}\text{U}$  isotope ratios of  
581 crustal material, rivers and products of hydrothermal alteration: new insights on the oceanic  
582 U isotope mass balance. *Isotopes in environmental and health studies*:1–23.

- 583 78. Eldhom O & Coffin MF (2000) Large igneous provinces and plate tectonics. *The history and*  
584 *dynamics of global plate motions*, (American Geophysical Union, Geophysical Monograph),  
585 Vol 121, pp 309–326.
- 586 79. Thordarson T & Self S (1996) Sulfur, chlorine and fluorine degassing and atmospheric loading  
587 by the Roza eruption, Columbia River Basalt Group, Washington, USA. *Journal of*  
588 *Volcanology and Geothermal Research* 74(1–2):49–73.
- 589 80. McManus J, *et al.* (2006) Molybdenum and uranium geochemistry in continental margin  
590 sediments: paleoproxy potential. *Geochimica et Cosmochimica Acta* 70(18):4643–4662.
- 591 81. Hood Av, *et al.* (2016) Integrated geochemical-petrographic insights from component-  
592 selective  $\delta^{238}\text{U}$  of Cryogenian marine carbonates. *Geology* 44(11):935–938.
- 593 82. Keller G, Han Q, Adatte T, & Burns SJ (2001) Palaeoenvironment of the Cenomanian–  
594 Turonian transition at Eastbourne, England. *Cretaceous Research* 22(4):391–422.
- 595 83. Wray DS & Gale AS (2006) The palaeoenvironment and stratigraphy of Late Cretaceous  
596 Chalks. *Proceedings of the Geologists' Association* 117(2):145–162.

597

598 **Supplementary Information**

599 **SI Materials and Methods**

600

601 **Reagents.** All reagents used were of ultra-high purity and prepared in-house by sub-boiling quartz  
602 and/or teflon distillation (HF, HNO<sub>3</sub>, HCl, CH<sub>3</sub>COOH) or purchased commercially from Thermo Fisher  
603 or Sigma Aldrich, NZ.

604

605 **Sample Preparation.** Weathered surfaces were removed from samples under dry conditions using a  
606 Dremel microdrill before sonication in high-purity Milli-Q water (>18.2 MΩ cm; Millipore, USA) to  
607 remove surface contaminants. Samples were dried in an oven at 40°C and then powdered in a laminar  
608 flow hood (Class 100; ISO 5) using an agate pestle and mortar, which was cleaned between samples  
609 using 99.995% SiO<sub>2</sub> sand and high-purity ethanol. Powdered samples, comprising 1–2 g, were subject  
610 to reductive-oxidative cleaning (63, 64) using 1 M hydrous hydrazine + 0.25 M citric acid in 16 M  
611 ammonia solution, followed by 1% H<sub>2</sub>O<sub>2</sub> in 0.1 M NaOH. Repeated MilliQ rinses were performed  
612 between cleaning steps. Such cleaning techniques remove potential contamination from residual  
613 organic matter and ferro-manganese coatings and are particularly important for extracting primary  
614 U/Ca ratios in foraminifera tests (63) and δ<sup>238</sup>U signatures from basalts (69). Cleaned powders were  
615 digested using 0.6 M or 1 M sodium acetate solution (buffered to a pH of 5) (70) at room temperature  
616 for 48 hrs in order to selectively digest carbonate phases and avoid U contributions from detrital  
617 silicates

618

619 **Ion Exchange Chemical Preparation of Samples for Uranium-Isotope Analysis.** Uranium-isotope  
620 composition was determined using a <sup>236</sup>U-<sup>233</sup>U double spike to correct for instrumental mass  
621 fractionation by adapting methods reported previously (20, 21, 23, 65, 66). The digest supernates  
622 were evaporated to dryness in the presence of excess 7 M HNO<sub>3</sub> to prevent the formation of sodium  
623 acetate precipitates. The final nitrate precipitates were then dissolved in 1.5 M HNO<sub>3</sub>. This digest was  
624 subsampled, diluted and analyzed via quadrupole ICP-MS using an Agilent 7500 instrument (Agilent  
625 Technologies, USA) at the Centre for Trace Element Analysis, University of Otago, New Zealand to  
626 determine the approximate U concentration in order to inform the double-spike addition calculation.  
627 Based on this U concentration, samples were again subsampled into PFA vials to achieve a total  
628 uranium mass of 30 to 150 ng and double spiked to give a <sup>236</sup>U/<sup>235</sup>U ratio of approximately 3. Solutions  
629 were refluxed for 24 hrs to ensure complete spike-sample equilibration. Due to the high matrix  
630 content of the carbonate digests, co-precipitation using pre-cleaned FeCl<sub>3</sub> and ammonia solution was  
631 conducted to remove the majority of Na and Ca from the sample and prevent overwhelming the ion-

632 exchange resin with matrix elements during the separation and purification of U. The resulting  
633 precipitates were separated from the high-matrix supernates through centrifugation and were then  
634 fully dissolved in 6 M HCl. After evaporation to dryness, the samples were re-dissolved in 3 M HNO<sub>3</sub>  
635 and loaded onto pre-cleaned heat shrink Teflon columns containing UTEVA resin (Eichrom  
636 Technologies, USA). Uranium separation and purification was achieved following previously published  
637 protocols (20, 21, 23, 65, 66). Samples were evaporated to dryness and oxidised using H<sub>2</sub>O<sub>2</sub> + HNO<sub>3</sub>  
638 for 24 hrs, to eliminate any organic residues from the resin, then evaporated once more. The purified  
639 U fractions were re-dissolved in 0.25 M HCl + 0.05 M HF in preparation for U isotope analysis. Uranium  
640 yields were typically > 95% and the total procedural blank was approximately 10–20 pg, which is  
641 negligible for U sample sizes of between 30 to 150 ng.

642

643 **Uranium-Isotope Analysis.** Uranium isotopic measurements were performed by multiple collector  
644 ICP-MS (MC-ICPMS) using a Nu-Plasma HR MC-ICPMS (Nu Instruments, UK) coupled to a DSN-100  
645 desolvation system, at the Centre for Trace Element Analysis, University of Otago, following previously  
646 published procedures (22, 23, 66). The <sup>238</sup>U/<sup>235</sup>U composition is presented in delta-notation (δ)  
647 following Eq. (1).

648

$$649 \quad \delta^{238}\text{U} = \left( \frac{(^{238}\text{U}/^{235}\text{U})_{\text{sample}}}{(^{238}\text{U}/^{235}\text{U})_{\text{CRM-145}}} - 1 \right) \times 1000 \quad (1)$$

650 The reference material CRM-145 (National Institute of Standards and Technology, U.S.A.) is  
651 the internationally recognized δ-zero standard (19) with a <sup>238</sup>U/<sup>235</sup>U ratio of 137.837 ± 0.015. Each  
652 sample δ<sup>238</sup>U value was calculated relative to two bracketing CRM145 standards, double spiked in the  
653 same way as samples, and with ion beam intensities matched to within 10%. Analytical uncertainties  
654 are given as twice the standard error (2SE), and reflect the internal instrumental error in the  
655 measurements of the sample and bracketing standards using standard techniques of error  
656 propagation (23). On average, 2SE was equivalent to ±0.07%, and is comparable to the external  
657 reproducibility (2SD) of repeat measurements of the same sample (21). Analytical performance has  
658 been verified previously, based on the analysis of certified reference materials (20-23, 66). Replicate  
659 analyses performed on samples within and between sessions showed excellent agreement, within the  
660 magnitude of their 2SE analytical uncertainties (Fig. S1).

661

662 **Elemental Composition Analysis.** For spiking purposes and in order to identify diagenetic alteration  
663 of samples, aliquots of samples were diluted appropriately and measured for their elemental  
664 concentrations by quadrupole ICP-MS at the Centre for Trace Element Analysis, University of Otago,

665 New Zealand. Suitable dilutions of a NIST traceable multi-element standard (Choice Analytical Pty Ltd,  
666 Australia) was used for instrumental calibration purposes, and an internal standard comprising a  
667 cocktail of 7 reference elements was added to all samples to correct for instrumental drift during  
668 measurement. The performance of the elemental analysis methods was checked by analysis  
669 of samples spiked with elements of interest. Average recoveries of  $102 \pm 4\%$  were obtained for the  
670 elements reported here. In addition to spiked samples the ICP-MS method has been validated by  
671 analysis of digested Basalt, Columbia River (BCR-2) and Basalt, Hawaiian Volcanic Observatory (BHVO-  
672 2) certified reference materials (USGS), recoveries averaged  $99\% \pm 5\%$ . A change in digestion protocol  
673 from 0.5 to 1M Sodium Acetate may have introduced variability in the U/Ca data, but does not affect  
674 the measured  $\delta^{238}\text{U}_{\text{carb}}$ . To minimise this effect, secular trends in elemental concentrations for  
675 Eastbourne and Raia del Pedale are identified using elemental composition data produced in a  
676 previously published study (35) where 5 mg powders were digested using 2 ml of 0.5 M acetic acid.  
677 Measurements were made using a Thermo Scientific Element 2 ICP-MS at the University of Oxford.

678

### 679 **Regression Analysis**

680 To capture the main features of the  $\delta^{238}\text{U}_{\text{carb}}$  dataset at Eastbourne, without placing undue emphasis  
681 on single outlying data points, a LOESS smoothing function has been applied to the U-isotope dataset  
682 (Fig. 1 and 2). This was performed using the 'ggplot2' package in R, with the 'geom\_smooth' function,  
683 a default polynomial setting of 2, and  $\alpha=0.15$ . This also calculates the 95% confidence interval of the  
684 LOESS regression. The majority of data points overlap with the 95% confidence interval of this  
685 regression (grey shading Fig. 1 and 2), if their analytical uncertainties are taken into account,  
686 suggesting that robust systematic trends can be identified. A smoothing function is not appropriate  
687 for the Raia del Pedale and South Ferriby datasets due to their lower sampling density and  
688 stratigraphic resolution.

689

690

691 **Model Description.**

692 **Summary.** The model is a simplified version of the GEOCARB and COPSE family of models (11, 13, 49-  
693 51), focusing on the shorter term carbon cycle processes. Normalized forcing parameters are:  
694 degassing (D) (linked to seafloor spreading rate), uplift driving erosion (E), and effects of vegetation  
695 and lithology on weatherability (W). The model is perturbed by an atmospheric CO<sub>2</sub> emission from LIP  
696 volcanism and calculates the response of the C, P and U cycles (Fig. S2). Briefly, silicate weathering  
697 responds to temperature and acts as a sink of C through carbonate burial, and a source of P and U to  
698 the ocean. Organic matter production is dependent on P concentrations, and acts as a sink for P and  
699 C. The extent of oceanic anoxia is controlled by O<sub>2</sub> supply and O<sub>2</sub> consumption through the  
700 remineralization of organic matter. Anoxic sediments act as a sink for U and C. P concentrations are  
701 also influenced by the extent of anoxia due to the redox sensitive burial of Fe-bound and organic-  
702 bound P. The U-isotope mass balance is then used to trace the extent of seafloor anoxia and the C-  
703 isotope mass balance to trace the relative proportion of organic C burial.

704

705 **Carbon and phosphorus cycles.** The model considers both inorganic and organic parts of the carbon  
706 cycle. The mass balance for the ocean-atmosphere reservoir of inorganic carbon (A) is given by:

707 
$$dA/dt = F_d - F_w + F_{ox} - F_{morg} - F_{torg} (+ F_{cw} - F_{cb}) + F_{LIP} \quad (2)$$

708 where the carbon fluxes are  $F_d$  = degassing at seafloor spreading centres,  $F_w$  = silicate weathering  
709 (followed by carbonate burial),  $F_{ox}$  = input of organic carbon from oxidative weathering and degassing,  
710  $F_{morg}$  = marine-derived organic-carbon burial, and  $F_{torg}$  = terrestrially derived organic-carbon burial.  
711 Carbonate weathering,  $F_{cw}$  is assumed to be balanced by a corresponding carbonate burial flux,  $F_{cb}$   
712 (i.e.  $F_{cb}=F_{cw}$ ) so these terms do not affect the dynamics.  $F_{LIP}$  is an additional carbon input perturbation  
713 due to LIP emplacement;  $F_{LIP} = 0$  at present.

714 For present-day fluxes (in  $10^{12}$  molC yr<sup>-1</sup>) the terms  $F_d = k_d = 8$ ,  $F_w = k_w = 8$ ,  $F_{ox} = k_{ox} = 9$ ,  $F_{morg} = k_{morg} =$   
715  $4.5$ ,  $F_{torg} = k_{torg} = 4.5$ , and  $F_{cb} = F_{cw} = k_c = 16$ , based on COPSE (and hence GEOCARB) are assigned. The  
716 present-day reservoir  $A_0 = 3.2 \times 10^{18}$  molC, giving a residence time with respect to silicate weathering  
717 removal of 400 thousand years (kyr), or with respect to silicate weathering plus organic-carbon burial  
718 of 188 kyr.

719 The degassing flux is given by:

720 
$$F_d = k_d * D \quad (3)$$

721 The silicate weathering flux is taken to depend on temperature, CO<sub>2</sub>, uplift, and the effects of  
722 vegetation and lithology (e.g. basalts versus granites) on weatherability:

$$723 \quad F_w = k_w * E * W * f(\text{CO}_2) * f(T) \quad (4)$$

724 Existing models assume that weathering is predominantly biotic by the mid-Cretaceous and therefore  
725  $f(\text{CO}_2)$  is the response of vegetation (rather than abiotic weathering) to CO<sub>2</sub> following Michaelis-  
726 Menten kinetics (after GEOCARB III). Here, CO<sub>2</sub> concentration is given in PAL, representing multiples  
727 of present atmospheric level:

$$728 \quad f(\text{CO}_2) = 2 * \text{CO}_2 / (1 + \text{CO}_2) \quad (5)$$

729 The proportion of inorganic carbon that resides in the atmosphere as CO<sub>2</sub> scales with total ocean-  
730 atmosphere inorganic carbon inventory (A)

$$731 \quad \text{CO}_2 = (A/A_0)^2 \quad (6)$$

732 The effect of changes in CO<sub>2</sub> and solar luminosity on temperature (from GEOCARB III) is:

$$733 \quad \Delta T = k_{\text{CO}_2} * \ln(\text{CO}_2) - k_{\text{SL}} * (t/570) \quad (7)$$

734 where  $k_{\text{CO}_2} = 4^\circ\text{C}$  (corresponding to a present-day climate sensitivity of about  $2.8^\circ\text{C}$  for doubling CO<sub>2</sub>)  
735 and  $k_{\text{SL}} = 7.4^\circ\text{C}$  for  $t$  in millions of years ago, which gives  $\sim 1.2^\circ\text{C}$  cooling at 94 Ma due to lower solar  
736 luminosity.

737 The dependence of weathering on temperature neglects temperature-driven changes in runoff and  
738 only considers the kinetic effect of temperature on mineral dissolution, which using an activation  
739 energy appropriate for granite is given by:

$$740 \quad f(T) = \exp(0.09 * \Delta T) \quad (8)$$

741 The input of organic carbon from oxidative weathering and degassing is kept constant for simplicity  
742 (although oxidative weathering depends on uplift and organic-carbon degassing depends on  
743 degassing):

$$744 \quad F_{\text{ox}} = k_{\text{ox}} \quad (9)$$

745 Terrestrial-derived organic-carbon burial is assumed to be fertilised by CO<sub>2</sub> (consistent with the  
746 weathering formulation):

$$747 \quad F_{\text{torg}} = k_{\text{torg}} * f(\text{CO}_2) \quad (10)$$

748 Marine-derived organic-carbon burial is taken to depend on ocean phosphorus concentration  
749 (normalized to modern values):

$$750 \quad F_{\text{morg}} = k_{\text{morg}} * (P/P_0) \quad (11)$$

751 Thus, to determine marine-derived organic-carbon burial the phosphorus cycle needs to be  
752 considered.

753 Phosphorus weathering is assumed to be tied to silicate weathering:

$$754 \quad F_{\text{Pw}} = k_{\text{Pw}} * (F_w/F_{w0}) \quad (12)$$

755 where  $k_{\text{Pw}} = 72 \times 10^9 \text{ molP yr}^{-1}$ .

756 The ocean P balance is given by:

$$757 \quad dP/dt = F_{\text{Pw}} - F_{\text{OrgP}} - F_{\text{FeP}} - F_{\text{CaP}} \quad (13)$$

758 where  $F_{\text{OrgP}}$  is burial associated with organic matter,  $F_{\text{FeP}}$  is burial adsorbed to iron oxides,  $F_{\text{CaP}}$  is burial  
759 associated with carbonate minerals. For present day fluxes ( $\times 10^9 \text{ molP yr}^{-1}$ ) we assign  $k_{\text{OrgP}} = 18$ ,  $k_{\text{FeP}} =$   
760  $18$ ,  $k_{\text{CaP}} = 36$ .

761 Organic phosphorus burial is sensitive to the anoxic fraction of the ocean,  $f_{\text{anoxic}}$ , given very different  
762  $(C/P)_{\text{organic}}$  burial ratios under anoxic ( $CP_{\text{anoxic}}=1000$ ) and oxic ( $CP_{\text{oxic}}=250$ ) bottom waters (52):

$$763 \quad F_{\text{OrgP}} = F_{\text{morg}} * ((f_{\text{anoxic}}/CP_{\text{anoxic}}) + ((1-f_{\text{anoxic}})/CP_{\text{oxic}})) \quad (14)$$

764 Iron oxide-bound P burial is also sensitive to the anoxic fraction of the ocean:

$$765 \quad F_{\text{FeP}} = k_{\text{FeP}} * (1-f_{\text{anoxic}}) \quad (15)$$

766 Calcium-bound phosphorus burial is assumed to scale with P input to sediments from sinking organic  
767 matter (with no redox dependence):

$$768 \quad F_{\text{CaP}} = k_{\text{CaP}} * (P/P_0) \quad (16)$$

769 The function defining the fraction of seafloor overlain by anoxic waters,  $f_{\text{anoxic}}$ , adopts a logistic  
770 functional form dependent on the balance between normalized oxygen demand ( $k_U * (P/P_0)$ ) and  
771 normalized oxygen supply ( $O_2/O_{20}$ ), where  $k_U$  represents the efficiency of nutrient utilization in  
772 upwelling regions:

$$773 \quad f_{\text{anoxic}} = 1 / (1 + e^{-k_{\text{anox}} * (k_U * (P/P_0) - (O_2/O_{20}))}) \quad (17)$$

774 Here,  $k_U = 0.5$  is chosen based on observations of high-latitude nutrient utilization and agreement  
 775 across a range of models (9, 59, 71, 72) that a transition from an oxic to an anoxic deep ocean occurs  
 776 at  $O_2/O_{20} \sim 0.5$  PAL (for present nutrient levels), or at  $P/P_0 \sim 2$  (for present  $O_2$  levels).  $k_{anox} = 12$  is chosen  
 777 based on observations that  $\sim 0.2$ – $0.3\%$  of the seafloor is overlain by anoxic bottom waters at present  
 778 (73), and model agreement that the transition from oxic to anoxic conditions is abrupt as, for example,  
 779  $O_2/O_{20}$  drops from  $\sim 0.6$  to  $\sim 0.4$  (9, 59, 72).

780 We make a simple consideration of the effect of increases in atmospheric  $O_2$  by integrating any  
 781 increases in organic-carbon burial above the initial steady state to give a cumulative input of  $O_2$ ,  
 782 calculating the resulting change in  $O_2/O_{20}$  (where the present  $O_{20} = 3.7 \times 10^{19}$  mol), and feeding this  
 783 change in  $O_2/O_{20}$  back into  $f_{anoxic}$ . We do not consider longer term negative feedbacks on  $O_2$  because  
 784 of the short interval under consideration here.

785 **Carbon-isotope mass balance.** The carbon-isotope mass balance follows the carbon mass balance:

$$786 \quad d(A \cdot \delta_A)/dt = F_d \cdot \delta_d + F_{ox} \cdot \delta_{ox} + F_{cw} \cdot \delta_{cw} + F_{LIP} \cdot \delta_{LIP} - (F_{morg} + F_{torg}) \cdot (\delta_A - \Delta) - (F_w + F_{cb}) \cdot \delta_A \quad (18)$$

787 The above equation can be simplified to:

$$788 \quad d(A \cdot \delta_A)/dt = F_{in} \cdot \delta_{in} + F_{LIP} \cdot \delta_{LIP} - F_{org}(\delta_A - \Delta) - F_{carb} \cdot \delta_A \quad (19)$$

789 where  $F_{in} = F_d + F_{ox} + F_{cw}$  is the total steady state input flux of carbon of mean isotopic composition  $\delta_{in}$   
 790 =  $-5 \text{ ‰}$  (as often assumed in other studies), the carbon input perturbation  $F_{LIP}$  has isotopic composition  
 791  $\delta_{LIP}$  (see sensitivity analysis below),  $F_{org} = F_{morg} + F_{torg}$  is the total burial flux of organic matter with  
 792 fractionation  $\Delta$  (taken here to be  $25 \text{ ‰}$ ) and  $F_{carb} = F_w + F_{cb}$  is the total burial flux of carbonates (with  
 793 no assumed C-isotope fractionation).

794 Simplifying equation (19) in the same manner ( $dA/dt = F_{in} + F_{LIP} - F_{org} - F_{carb}$ ), then applying the product  
 795 rule ( $d(A \cdot \delta_A)/dt = A \cdot d\delta_A/dt + \delta_A \cdot dA/dt$ ) and substituting and rearranging gives:

$$796 \quad d\delta_A/dt = (F_{in} \cdot (\delta_{in} - \delta_A) + F_{LIP} \cdot (\delta_{LIP} - \delta_A) - F_{org} \cdot (-\Delta))/A \quad (20)$$

797 With no perturbation ( $F_{LIP} = 0$ ) at steady state ( $d\delta_A/dt = 0$ ) this corresponds to the widely-used  
 798 formulation:

$$799 \quad \delta_A = \delta_{in} + f \cdot \Delta \quad (21)$$

800 Where 'f' is the fraction of carbon buried in organic form i.e.  $f = F_{org}/F_{in} = F_{org}/(F_{org} + F_{carb})$ . For the  
 801 modern fluxes suggested above  $f = 9/33 = 0.273$  and  $\delta_A \sim 1.8 \text{ ‰}$  if  $\Delta = 25$ .

## 802 Uranium-isotope mass balance

803 The U-cycle model assumes that the riverine input of U is driven by silicate weathering, all U sinks  
804 scale linearly with U concentration, the hydrothermal sink of U also scales with degassing from  
805 seafloor spreading (D), and the anoxic sink of U also scales with  $f_{\text{anoxic}}$ , the fraction of anoxic seafloor:

$$806 \quad dU/dt = F_{\text{riv}} - F_{\text{hyd}} - F_{\text{anoxic}} - F_{\text{carbonate}} - F_{\text{suboxic}} - F_{\text{oxic metals}} \quad (22)$$

$$807 \quad F_{\text{riv}} = k_{\text{riv}} * F_w / F_{w0} \quad (23)$$

$$808 \quad F_{\text{hyd}} = k_{\text{hyd}} * D * (U/U_0) \quad (24)$$

$$809 \quad F_{\text{anoxic}} = k_{\text{anoxic}} * (U/U_0) * f_{\text{anoxic}} / f_{\text{anoxic0}} \quad (25)$$

$$810 \quad F_{\text{carbonate}} + F_{\text{suboxic}} + F_{\text{oxic metals}} = F_{\text{other}} = k_{\text{other}} * (U/U_0) \quad (26)$$

811 For a modern  $U=1.85 \times 10^{13}$  mol, we use estimates of  $k_{\text{anoxic}} = 6.2 \times 10^6$  mol yr<sup>-1</sup>,  $k_{\text{hyd}} = 5.7 \times 10^6$  mol yr<sup>-1</sup>,  
812  $k_{\text{other}} = 36 \times 10^6$  mol yr<sup>-1</sup>, and therefore  $k_{\text{riv}} = 47.9 \times 10^6$  mol yr<sup>-1</sup> (16, 19). The corresponding isotope mass  
813 balance is:

$$814 \quad d\delta_U/dt = (F_{\text{riv}} * (\delta_{\text{riv}} - \delta_U) - F_{\text{hyd}} * \Delta_{\text{hyd}} - F_{\text{anoxic}} * \Delta_{\text{anoxic}} - F_{\text{other}} * \Delta_{\text{other}}) / U \quad (27)$$

815 (Note here that  $\Delta$  are all positive for U isotopes, in contrast to  $\Delta$  for C isotope fractionation.) For the  
816 modern (18, 19, 30, 54) we assume  $\delta_{\text{riv}} = -0.29$ ,  $\Delta_{\text{hyd}} = 0.2$ ,  $\Delta_{\text{anoxic}} = 0.5$ , and  $\delta_U = -0.39$ , requiring  $\Delta_{\text{other}} =$   
817 0.0156 for steady state.

818

## 819 Mid-Cretaceous model initialisation, U cycle assumptions and perturbation scenarios

820 **Boundary conditions:** The mid-Cretaceous had elevated rates of seafloor spreading and  
821 corresponding degassing, with  $D=1.5$ , as used in GEOCARB/COPSE models. At the time of OAE 2, an  
822 increase in hydrothermal input by 20% has been estimated to be consistent with an observed Sr-  
823 isotope shift (8, 74) hence we use  $D=1.8$  as the baseline value. Uplift was considerably lower in the  
824 mid-Cretaceous than at present, with  $E=0.7$  from GEOCARB/COPSE used as a baseline. The rise of  
825 angiosperms is assumed to have finished increasing weathering rates by 100 Ma, following  
826 GEOCARB/COPSE. Basalt area is estimated to be comparable to today (75). Therefore, present  
827 weatherability  $W = 1$  is used as a baseline. Lower solar luminosity at 94 Ma translates to 1.2°C of  
828 cooling. Higher steady-state atmospheric O<sub>2</sub> is considered as part of our sensitivity analysis.

829 **U Isotope Fractionation Factor:** The sensitivity of changes in calculated  $\delta^{238}\text{U}_{\text{sw}}$ , in terms of  
830 reflecting the degree of anoxia, is dependent on the assumed magnitude of fractionation during U  
831 reduction between anoxic sediments and seawater ( $\Delta_{\text{anoxic}}$ ). Modern observational, theoretical and  
832 experimental data suggest that the reduction of U(VI) to U(IV) is associated with a positive U-isotope  
833 fractionation factor of between 0.4 to 1.3 ‰ (14, 19, 20, 23-25, 30, 76) where the apparent  
834 enrichment factor in natural settings may be highly variable and dependent on local geochemical and  
835 depositional conditions (18, 20, 30), which are hard to quantify on a global scale during Earth's history.  
836 To this end, previous mass balance models for the Permo-Triassic mass extinction and OAE 2 have  
837 employed various enrichment factors of +0.5 (14, 26), +0.6 (28) and +0.77 ‰ (29), which generate  
838 significantly different estimates for the size of anoxic sinks, and hence seafloor area covered by anoxic  
839 waters, required to drive a given negative  $\delta^{238}\text{U}$  excursion. The assumption of  $\Delta_{\text{anoxic}}$  remains a  
840 fundamental limitation for the interpretation of ancient  $\delta^{238}\text{U}$  data. Due to this uncertainty, we use  
841 the observed difference in  $\delta^{238}\text{U}$  between contemporaneous anoxic shales (ODP site 1261, Fig. 1)  
842 where the average post-OAE value reported for ODP 1262 is 0.063‰ (14) and Eastbourne is -0.45‰,  
843 giving a  $\Delta_{\text{anoxic}}$  of +0.51‰, which is within the range of observational data from modern anoxic basins  
844 (14, 19, 20, 23-25, 30, 76). Sensitivity analysis (Table S2) demonstrates that increasing  $\Delta_{\text{anoxic}}$  to 0.6‰,  
845 would increase the magnitude of the negative  $\delta^{238}\text{U}_{\text{sw}}$  excursion by 0.1‰ for the same  $\text{CO}_2$  emission  
846 scenario and size of anoxic sinks. To match the observed excursions in Eastbourne when  $\Delta_{\text{anoxic}} = 0.6‰$   
847 then requires a decrease in the perturbation magnitude, and lower estimates of the area of seafloor  
848 anoxia of 4 to 10%. If  $\Delta_{\text{anoxic}}$  were assumed to be much larger this drives the steady state  $\delta^{238}\text{U}_{\text{sw}}$  lower  
849 than the range recorded at Eastbourne and is not deemed plausible without invoking unrealistically  
850 high  $\delta_{\text{riv}}$  values, or invoking a diagenetic offset for which there is no evidence. It would also require  
851 smaller changes to the carbon cycle model, with a smaller  $\text{CO}_2$  emission, temperature increase and  
852 relative change in productivity, in order to drive the same magnitude of  $\delta^{238}\text{U}$  excursion. The result of  
853 this would be to decrease the amount of carbon removed from the ocean-atmosphere system through  
854 productivity and burial under anoxic conditions, and therefore create a decrease in the magnitude of  
855 the calculated positive CIE. Using a  $\Delta_{\text{anoxic}}$  of +0.5‰ generates a good agreement between the model  
856 outputs for temperature and estimates from proxy reconstructions, and produces a  $\delta^{13}\text{C}$  excursion  
857 that is only ~0.5‰ lower than observed at Eastbourne. Thus we do not consider the higher  
858 fractionation factor/smaller perturbation scenario to be realistic for OAE 2. The internally consistent  
859 carbon cycle model therefore helps increase the confidence in our interpretation of the area of  
860 seafloor that was overlain by an anoxic water column.

861 **U riverine input:** The modern average measured riverine  $\delta^{238}\text{U}$  composition ( $\delta_{\text{riv}}$ ) is  
862 indistinguishable from bulk silicate earth (BSE) at -0.29‰ (18, 19, 21, 54, 69, 77). In the mid-

863 Cretaceous setup of the C–P–U model (see below),  $\delta_{riv}$  is set to  $\sim -0.19\text{‰}$  in order to generate  $\delta^{238}\text{U}_{sw}$   
864 values in agreement with the  $\delta^{238}\text{U}_{carb}$  data from Eastbourne under different atmospheric  $\text{O}_2$  scenarios.  
865 Although this value is slightly higher than modern average  $\delta_{riv}$  it is a plausible figure given the  
866 uncertainty of exposed weatherable lithologies on land. Indeed, it has been suggested that  $\delta_{riv}$  could  
867 vary by up to a few per mil for different periods of Earth’s history (28) although estimates are limited  
868 by substantial uncertainties including the paleogeology reconstructions, degree of soil development,  
869 vegetation cover and changing weathering regimes. The chosen value used here for  $\delta_{riv}$  is also within  
870 the range back-calculated through mass-balance modelling of the modern U cycle ( $\delta_{riv} = -0.18$  to  $-0.28$   
871  $\text{‰}$ ), which encompasses the uncertainty of the size and isotopic composition of modern U sinks (19).  
872 Thus, using either the modern  $\delta_{riv}$  that is close to BSE, or a slightly higher  $\delta_{riv}$  of  $-0.19 \text{‰}$  makes little  
873 difference within the uncertainty of the current characterization of U sinks.

874 **Resulting steady state:** With these changes in boundary conditions (at  $\text{O}_2 = 1$ ) the predicted  
875  $A/A_0 = 1.63$ ,  $\text{CO}_2 = 2.7 \text{ PAL}$  and  $\Delta T = +2.7^\circ\text{C}$  (i.e. global average  $T \sim 18^\circ\text{C}$ ), comparing well with GEOCARB  
876 III and the warmer world at the time. Predicted  $P/P_0 = 1.43$ , which assuming present  $\text{O}_2$  generates  
877 more anoxia ( $f_{anoxic} = 0.03$ ).  $\delta^{13}\text{C} \sim +3.2 \text{‰}$  is predicted thanks to elevated terrestrial and marine  
878 organic-carbon burial (consistent with data from Eastbourne and South Ferriby). These changes in  
879 boundary conditions lead to a predicted increase in U river input outweighed by an increase in the  
880 anoxic sink, leading to a predicted decrease in ocean U content to  $0.9 \times 10^{13} \text{ mol}$  (50% of present), and  
881 when  $\delta_{riv} = -0.19$  and  $\Delta_{anoxic} = 0.5$  this gives a predicted  $\delta_U = -0.53 \text{‰}$ .

882 **LIP  $\text{CO}_2$  injection:** A carbon cycle perturbation associated with the emplacement of the  
883 Caribbean-Columbian, Madagascar and/or other LIPs close to the Cenomanian/Turonian boundary  
884 has been hypothesized as the trigger for OAE 2. These two LIPs are each estimated at  $4.5 \times 10^6 \text{ km}^3$   
885 basalt (78) equivalent to mass  $1.3 \times 10^7 \text{ Gt}$  (density  $2.9 \text{ g cm}^{-3}$ ) that, assuming  $2.0 \text{ wt\% CO}_2$  (79), yields  
886  $2.6 \times 10^5 \text{ GtCO}_2$  or  $7.1 \times 10^4 \text{ GtC}$  or  $5.91 \times 10^{18} \text{ molC}$ . This figure gives a combined total carbon pool that  
887 could be degassed throughout the emplacement of these two LIPs of  $\sim 12 \times 10^{18} \text{ molC}$ . The nature and  
888 corresponding rate of degassing is uncertain. We consider release events of  $\sim 10\text{--}20\%$  of the total as  
889 plausible (i.e.  $1.2\text{--}2.4 \times 10^{18} \text{ molC}$ ), which over 150 kyr amounts to  $0.8\text{--}1.6 \times 10^{13} \text{ molC yr}^{-1}$ , up to a  
890 doubling of the degassing flux. Clearly multiple perturbations of approximately this magnitude could  
891 have occurred during the full interval of LIP emplacement.

892 If the prescribed  $\text{CO}_2$  injection is assumed to be solely mantle derived with a  $\delta^{13}\text{C}$  signature of  
893  $-5\text{‰}$ , then a minor negative CIE (of  $\sim 1\text{‰}$ ) before the positive CIE of OAE 2 is predicted (Table 2).  
894 However, there is little indication of this feature in the  $\delta^{13}\text{C}$  record for OAE 2, unlike other similar  
895 events such as the early Aptian OAE 1a ( $\sim 120 \text{ Ma}$ ) (1), suggesting either a slower initial rate of  $\text{CO}_2$

896 emission for OAE 2, where the potential negative excursion was counterbalanced by the burial of  
897 organic matter, or that the degassed volatiles contained a mixture of mantle-derived and assimilated  
898 carbonate C from overlying crustal material. Because of this potential complication, the injected  
899 carbon is assumed to have a  $\delta^{13}\text{C}$  signature of 0‰ in the model runs shown in Fig. 3. Due to the  
900 inherent delay in the carbon cycle between the timing of the  $\text{CO}_2$  injection and maximum extent of  
901 oceanic anoxia, the maximum  $\delta^{13}\text{C}$  predicted for the subsequent positive CIE is less sensitive to this  
902 assumed input  $\text{CO}_2$  signature, with only  $\sim 0.1\%$  difference between the two scenarios (Table S2).

903 **Sensitivity analyses.** A series of sensitivity analyses show that decreasing background  $\text{CO}_2$   
904 degassing (D), uplift and erosion rates (E), or the weatherability of exposed landmasses (W), leads to  
905 reduced levels of anoxia during the pre-OAE 2 interval and therefore higher predicted values of  
906  $\delta^{238}\text{U}_{\text{sw}}$ . Such boundary conditions make the calculated changes in anoxia, [U],  $\delta^{238}\text{U}_{\text{sw}}$  and  $\delta^{13}\text{C}$  less  
907 sensitive to the same  $\text{CO}_2$  perturbation. Importantly, for reasonable initial boundary conditions that  
908 are consistent with more complex biogeochemical models, geologically plausible magnitudes of  $\text{CO}_2$   
909 increases can drive expanded anoxia, and inferred  $\delta^{238}\text{U}_{\text{sw}}$  changes in all cases. In a first set of model  
910 sensitivity analyses (Table S1) we vary the model boundary conditions of D, E, W, and atmospheric  $\text{O}_2$   
911 over plausible ranges. We consider  $D=1.5$  as a lower limit (no extra increase in hydrothermal activity)  
912 and  $D=2.1$  (symmetric perturbation) as an upper limit. E is varied over  $\pm 0.2$ , which spans most of the  
913 Phanerozoic range (13). W is varied over  $\pm 0.2$  given uncertainty in the effect of angiosperms on  
914 weathering and in the background area of volcanic rocks at the time (75). For atmospheric  $\text{O}_2$  following  
915 recent work (53) we only consider increases and we limit these to a level (1.2 PAL) that returns  
916 modern levels of ocean anoxia (given evidence for more widespread anoxia prior to OAE2). These  
917 changes in boundary conditions alter the initial steady state and the core dynamics of the model, and  
918 we examine how this changes the response to a common  $\text{CO}_2$  injection perturbation of  $1.8 \times 10^{18}$  molC  
919 over 150 kyr ( $1.2 \times 10^{13}$  molC/yr). In a second set of sensitivity analyses (Table S2) we take the same  
920 perturbation experiment from standard boundary conditions with  $\text{O}_2 = 1$  PAL and vary the assumed  
921  $\delta^{13}\text{C}$  of LIP  $\text{CO}_2$  input, and  $\delta_{\text{riv}}$  and  $\Delta_{\text{anoxic}}$  in the U isotope system. These changes only affect the isotopic  
922 expression of the modelled C, P, U changes.

## 923 **SI Discussion**

924 Primary biotic and abiotic calcite and aragonite precipitates have been shown to record ambient  
925 solution  $\delta^{238}\text{U}$  values accurately with minimal fractionation, despite structural co-ordination changes  
926 with regard to calcite precipitation (21, 25, 31, 32). These studies also suggest that there is no  
927 appreciable fractionation driven by biotic ‘vital effects’, consistent with the fact that U does not serve  
928 a biological function. A minor positive fractionation factor has been observed for abiotic aragonite  
929 formation under very specific experimental conditions, whereby the solid phase has a more positive

930  $\delta^{238}\text{U}$  than the residual solution (32) although the applicability of these experimental results to real-  
931 world conditions is still not well understood. This complication could only have potentially effected  
932 Raia del Padale, which was originally comprised of mixed aragonite and calcite that is typical of  
933 shallow-water platform settings. U concentrations are also vastly different between calcite and  
934 aragonite, with aragonite being up to two orders of magnitude greater. This difference is clearly seen  
935 in the greater U/Ca ratios of the Raia del Pedale carbonates (Fig. 1) and the mixed mineralogy of this  
936 section could also explain the greater degree of scatter. Despite this the general trends in U/Ca are  
937 replicated at the two sites.

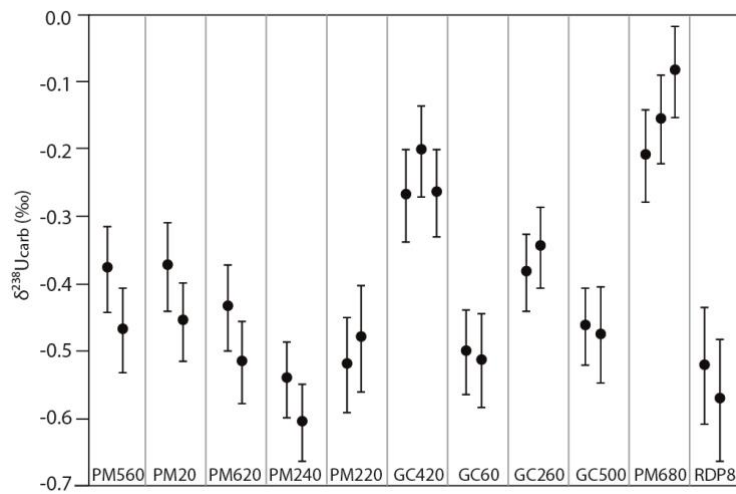
938 Diagenesis is an important consideration for understanding any geochemical dataset,  
939 especially in carbonates that can undergo extensive syn- and post-depositional recrystallization. The  
940 redox-sensitive nature of U also introduces additional complications in the diagenetic environment. U  
941 mobility in sediments is heavily influenced by local reduction and diffusion within pore waters (18, 31,  
942 80) and secondary U can be incorporated into diagenetic cements or into neomorphosed carbonates  
943 (31, 81). This process has been demonstrated for individual carbonate cements (81) and for bulk  
944 samples from modern carbonate cores which tend to show a positive  $\delta^{238}\text{U}$  offset compared to  
945 contemporary seawater (31). Negative  $\delta^{238}\text{U}$  offsets have also been measured in some dolomitized  
946 carbonates (21, 31). The reason for this is poorly understood but it may be due to either the influence  
947 of meteoric waters with more negative  $\delta^{238}\text{U}$  signatures, or alteration under hypersaline conditions  
948 (21, 31).

949 The influence of pore-water reduction and syn-sedimentary recrystallization or cementation  
950 should be lowest in the Eastbourne Chalk section, which is thought to have had an oxygenated water  
951 column during deposition, with very low total organic carbon (TOC; less than 0.15% (82)) and no  
952 appreciable sulphate reduction in pore waters (33). The impact of later stage diagenesis should be  
953 minimal at Eastbourne, with the stable low-magnesium calcite mineralogy characteristic of pelagic  
954 calcifiers that is more resistant to diagenetic alteration (83). This supposition is confirmed by the lack  
955 of correlation between  $\delta^{238}\text{U}$  with [U] or Mn/Ca and Sr/Ca (Fig. S3). Indeed, Eastbourne has been  
956 widely used as a reference section for many isotopic systems because of the exemplary nature of the  
957 archive. It is encouraging that major changes in  $\delta^{238}\text{U}$  are not dependent on lithology, and also cross  
958 major lithology transitions. In general the  $\delta^{238}\text{U}_{\text{carb}}$  data during the OAE 2 interval show systematic  
959 trends that correspond to hypothesised changes in other environmental parameters. Preceding the  
960 CIE of OAE 2, however, is a negative  $\delta^{238}\text{U}_{\text{carb}}$  excursion that corresponds to a U/Ca decrease. We do  
961 not focus on this excursion, however it is plausibly related to observed cyclic black shales that precede  
962 OAE 2 and thought to represent anoxia driven by orbital variability (68).

963 Carbonate samples from South Ferriby also show little geochemical evidence for  
964 recrystallization (Fig. S3) although the section is generally more lithified than Eastbourne. The  
965 presence of the distinct black shale (the so-called 'Black Band') above the unconformity raises some  
966 concerns. Potentially, U mobilization from the organic-rich level could explain the positive  $\delta^{238}\text{U}$   
967 excursion seen in South Ferriby. The highest  $\delta^{238}\text{U}_{\text{carb}}$  in this section also correspond to the highest  
968 Mn/Ca ratios, suggesting the influence of pore water U reduction.

969 In contrast to the pelagic sites, Raia del Pedale has undergone extensive recrystallization, with  
970 evidence for interaction with meteoric waters coming from depleted Sr/Ca and, in places, high Mg/Ca  
971 indicative of dolomitization. In particular, the three lowest  $\delta^{238}\text{U}$  values in Raia del Pedale are from  
972 samples with higher Mg/Ca and anomalously high U/Ca ratios (Fig. 1, Fig. S3), consistent with an  
973 observed negative isotopic shifts between modern dolomites and seawater (21, 31). These low values  
974 however, form a negative excursion that appears to correlate with the Eastbourne  $\delta^{238}\text{U}_{\text{carb}}$  data  
975 during the more variable pre-OAE 2 interval (Fig. 1). Further investigation of pre-OAE 2 U-isotopes are  
976 required to test if this excursion is primary. The anomalously high  $\delta^{238}\text{U}_{\text{carb}}$  values within the OAE 2  
977 interval at Raia del Pedale are more typical of signatures found in anoxic shales and may potentially  
978 indicate extensive early diagenetic alteration and secondary incorporation of U from *in situ* organic-  
979 matter degradation. Interestingly, Mn is not enriched in these samples, as would be expected due to  
980 alteration under reducing pore waters. These high  $\delta^{238}\text{U}_{\text{carb}}$  values are, however, restricted to a few  
981 samples only, suggesting that these potential geochemical impacts were probably spatially limited.  
982

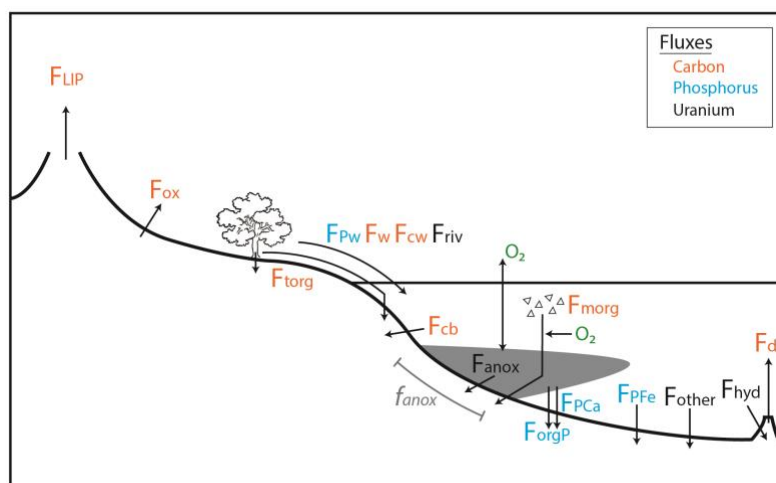
983 **Supplementary Figures**



984

985 Fig. S1: Replicate measurements performed on multiple samples between analysis sessions.

986 Uncertainty shown as 2 SE.



987

988 Fig. S2. Schematic illustrating coupled model fluxes of the C–P–U cycles with reference to the  
989 variables defined in the text.

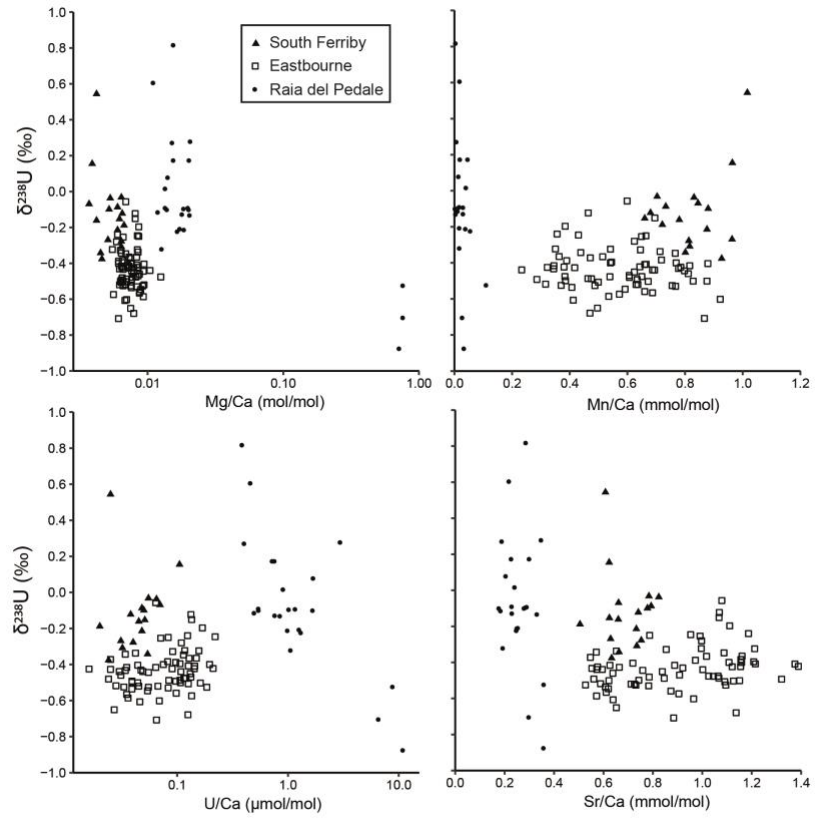
990

991

992

993

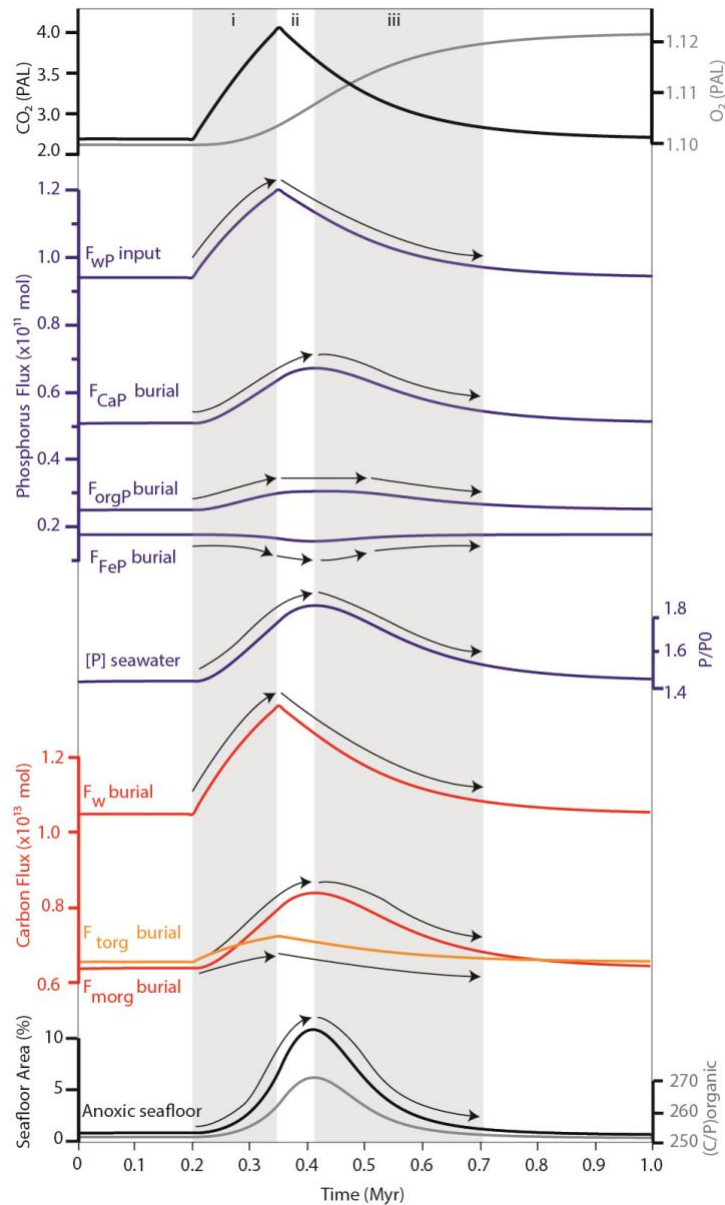
994



995

996 Fig. S3: Cross plots of  $\delta^{238}\text{U}$  against geochemical indicators of diagenesis.

997



998

999 Fig. S4: C–P–U model outputs for a single expansion of anoxia under the  $O_2 = 1.1$  scenario with a  $CO_2$   
 1000 emission of  $1.05 \times 10^{13}$  mol C yr<sup>-1</sup> for 150 kyrs. See model description and main text for element flux  
 1001 symbols. The behaviour of the C and P cycles can be divided into three stages related to the  
 1002 development of anoxia: i) the onset of deoxygenation; ii) peak extent of anoxia; and iii)  
 1003 reoxygenation. C and P fluxes are separated and the arrows highlight the behaviour of each flux  
 1004 across the three stages. Specifically, a decoupling of [P] and P inputs ( $F_{wp}$ ) in stage (ii) is related to  
 1005 changes in the C/P ratio and burial of organic bound P ( $F_{orgP}$ ) and Fe bound P ( $F_{FeP}$ ). The minor  
 1006 increase in atmospheric  $O_2$ , due to the burial of organic carbon, is also shown. These internal P  
 1007 dynamics create the delay in the maximum extent of anoxia compared to the atmospheric  $CO_2$   
 1008 increase and also facilitate reoxygenation as  $CO_2$  decreases.

1009

**Table S1. Sensitivity analysis varying the model boundary conditions** (with a common  $1.8 \times 10^{18}$  molC perturbation over 150 kyr with  $\delta_{LIP} = 0$  ‰). Boxed rows highlight boundary conditions used in the main text.

Initial conditions				Initial steady-state outputs						Maximum excursion outputs					
D	E	W	O <sub>2</sub> /O <sub>20</sub>	CO <sub>2</sub>	P/P <sub>0</sub>	U/U <sub>0</sub>	f <sub>anoxic</sub>	δ <sup>13</sup> C	δ <sub>U</sub>	CO <sub>2</sub>	P/P <sub>0</sub>	U/U <sub>0</sub>	f <sub>anoxic</sub>	δ <sup>13</sup> C	δ <sub>U</sub>
1	1	1	1	1	1	1	0.003	1.82	-0.39*	1.82	1.69	0.35	0.12	3.82	-0.87*
1.8	0.7	1.0	1.0	2.68	1.43	0.50	0.031	3.23	-0.53	4.26	2.45	0.03	0.92	5.54	-1.01
1.8	0.7	1.0	1.1	2.69	1.42	0.91	0.009	3.21	-0.39	4.28	1.95	0.20	0.17	4.35	-0.88
1.8	0.7	1.0	1.2	2.69	1.41	1.18	0.003	3.20	-0.30	4.29	1.89	0.78	0.04	4.22	-0.52
1.5	0.7	1.0	1.0	2.24	1.22	0.82	0.009	2.91	-0.39	3.53	1.68	0.27	0.12	4.19	-0.89
2.1	0.7	1.0	1.0	3.12	1.67	0.20	0.120	3.57	-0.63	4.79	2.86	0.03	0.99	6.00	-0.87
1.8	0.5	1.0	1.0	4.42	1.35	0.63	0.019	3.50	-0.47	6.63	1.76	0.15	0.18	4.34	-0.85
1.8	0.9	1.0	1.0	1.92	1.49	0.40	0.046	3.02	-0.56	3.14	2.74	0.03	0.99	5.77	-1.01
1.8	0.7	0.8	1.0	3.70	1.37	0.59	0.023	3.41	-0.49	5.68	1.90	0.08	0.33	4.53	-0.93
1.8	0.7	1.2	1.0	2.10	1.47	0.43	0.041	3.08	-0.55	3.41	2.67	0.03	0.98	5.73	-1.01

\*Note: U-isotope system set up for the modern with  $\delta_{riv} = -0.29$ . All other scenarios assume  $\delta_{riv} = -0.19$

1013

**Table S2. Sensitivity analysis varying the model isotopic assumptions.** Using standard boundary conditions of  $D=1.8$ ,  $E=0.7$ ,  $W=1.0$ ,  $O_2=1.0$ , and a common  $1.8 \times 10^{18}$  molC perturbation over 150 kyr.

Input assumptions			$\delta^{13}\text{C}$			$\delta^{238}\text{U}_{\text{sw}}$			
$\delta^{13}\text{C}$ LIP	$\delta^{238}\text{U}_{\text{river}}$	$\Delta_{\text{anoxic}}$	initial	min	max	initial	min	max	Final
<b>-5</b>			3.23	2.26	5.41				
<b>0</b>			3.23	2.96	5.54				
<b>-10</b>			3.23	1.44	5.29				
	<b>-0.19</b>	<b>0.5</b>				-0.53	-1.01	-0.31	-0.48
	<b>-0.29</b>	0.5				-0.63	-1.11	-0.41	-0.58
	<b>-0.09</b>	0.5				-0.43	-0.91	-0.21	-0.38
	-0.19	<b>0.4</b>				-0.46	-0.85	-0.29	-0.43
	-0.19	<b>0.6</b>				-0.59	-1.17	-0.33	-0.53

1014

1015

## 1016 Data Tables

Eastbourne U-isotope data and trace element ratios performed on 0.6 or 1 M Sodium Acetate leachates. Li-isotope data after ref 8 and this study. Heights from base of section.									
Sample Name	Height (cm)	$\delta^{238}\text{Ucarb}$ (‰)	2SE	Mg/Ca (mol/mol)	Sr/Ca (mmol/mol)	Mn/Ca (mmol/mol)	U/Ca ( $\mu\text{mol/mol}$ )	$\delta^7\text{Li}$ (‰)	2SD
GC600	0	-0.559	0.065	0.009	0.873	0.660	0.098		
GC580	20	-0.477	0.057	0.008	1.045	0.539	0.115		
GC560	40	-0.366	0.057	0.008	1.017	0.514	0.128		
GC540	60	-0.197	0.085	0.009	1.111	0.384	0.169		
GC500	100	-0.470	0.071	0.009	0.908	0.606	0.133	19.1	0.6
GC460	140	-0.123	0.057	0.008	1.069	0.464	0.133		
GC440	160	-0.451	0.066	0.008	0.838	0.624	0.131		
GC420	180	-0.246	0.068	0.008	0.953	0.430	0.220		
GC400	200	-0.488	0.068	0.008	0.846	0.475	0.084	20.3	0.2
GC380	220	-0.679	0.048	0.008	1.137	0.470	0.125		
GC360	240	-0.476	0.063	0.008	1.064	0.383	0.120		
GC300	300	-0.487	0.059	0.007	1.067	0.463	0.106	19.2	0.9
GC260	340	-0.365	0.057	0.007	1.161	0.363	0.149		
GC200	400	-0.423	0.068	0.007	1.155	0.380	0.143		
GC160	440	-0.388	0.065	0.006	0.972	0.389	0.097		
GC120	480	-0.323	0.065	0.006	0.996	0.350	0.117		
GC100	500	-0.240	0.087	0.006	1.187	0.356	0.124	23.9	0.1
GC60	540	-0.507	0.069	0.006	1.091	0.499	0.126		
GC40	560							<b>20.6</b>	<b>0.4</b>
GC00	600	-0.280	0.052	0.006	0.997	0.624	0.109	11.2	0.5
PM20	620	-0.416	0.059	0.006	0.888	0.816	0.064		
PM40	640	-0.328	0.059	0.006	0.854	0.645	0.091		
PM60	660	-0.526	0.066	0.009	1.095	0.755	0.185	<b>11.9</b>	<b>0.0</b>

PM100	700							7.4	0.7
PM120	720	-0.400	0.071	0.008	1.159	0.541	0.196		
PM140	740	-0.503	0.067	0.007	1.126	0.672	0.162		
PM180	780	-0.347	0.060	0.007	1.088	0.766	0.114		
PM200	800							<b>8.7</b>	<b>0.1</b>
PM220	820	-0.501	0.070	0.006	1.151	0.876	0.107		
PM240	840	-0.574	0.057	0.006	0.905	0.572	0.135		
PM260	860	-0.602	0.068	0.007	0.965	0.922	0.069		
PM280	880	-0.708	0.060	0.006	0.884	0.867	0.065		
PM300	900	-0.408	0.065	0.007	1.215	0.665	0.126	5.9	0.4
PM340	940	-0.400	0.071	0.006	1.108	0.769	0.075	<b>10.7</b>	<b>0.3</b>
PM360	960	-0.057	0.092	0.007	1.079	0.599	0.064		
PM400	1000	-0.431	0.058	0.006	0.921	0.777	0.047	9.9	0.6
PM420	1020	-0.324	0.080	0.008	1.212	0.541	0.157		
PM440	1040	-0.396	0.064	0.007	1.208	0.545	0.106		
PM480	1080	-0.254	0.060	0.007	0.991	0.649	0.071		
PM500	1100	-0.409	0.060	0.008	1.375	0.660	0.144	15.3	0.4
PM520	1120	-0.384	0.059	0.006	1.156	0.718	0.082		
PM540	1140	-0.493	0.061	0.008	1.321	0.634	0.097		
PM560	1160	-0.424	0.063	0.007	1.121	0.785	0.090	<b>13.1</b>	<b>0.4</b>
PM580	1180	-0.422	0.082	0.008	1.389	0.643	0.211		
PM600	1200							8.3	0.5
PM620	1220	-0.476	0.061	0.012	1.026	0.650	0.117	10.2	0.4
PM640	1240	-0.440	0.082	0.010	1.002	0.694	0.108	22.8	0.4
PM680	1280	-0.151	0.068	0.008	1.068	0.695	0.135		
PM720	1320	-0.404	0.068	0.009	0.719	0.879	0.044		
PM740	1340	-0.250	0.060	0.009	0.787	0.664	0.083		
PM760	1360	-0.444	0.067	0.009	0.759	0.798	0.055	<b>22.5</b>	<b>0.1</b>

WC0	1390	-0.520	0.101	0.009	0.725	0.630	0.067	20.9	0.2
PM800	1400	-0.530	0.075	0.008	0.783	0.767	0.083		
W0.2	1410							<b>21.8</b>	<b>0.2</b>
WC200	1440							17.7	0.7
W0.6	1450	-0.546	0.071	0.009	0.620	0.592	0.054		
W0.8	1470								
W1	1490	-0.460	0.069	0.009	0.638	0.811	0.031	15.7	0.5
W1.2	1510							<b>13.1</b>	<b>0.2</b>
W1.4	1530	-0.566	0.069	0.009	0.611	0.687	0.035		
WC300	1540							14.5	0.6
W1.6	1550	-0.439	0.071	0.008	0.595	0.687	0.030		
W2	1590	-0.337	0.065	0.008	0.652	0.713	0.042	17.8	0.2
W2.4	1630	-0.586	0.075	0.009	0.572	0.535	0.036		
W2.8	1670	-0.481	0.074	0.006	0.785	0.607	0.024		
W3	1690							22.5	0.3
W3.2	1710	-0.520	0.066	0.006	0.712	0.636	0.045		
W3.6	1750	-0.501	0.077	0.007	0.622	0.828	0.044		
W4	1790	-0.526	0.084	0.007	0.731	0.487	0.055	20.7	0.6
W4.4	1830	-0.499	0.073	0.007	0.743	0.385	0.039		
WC600	1840							23.8	0.6
W4.8	1870	-0.651	0.078	0.007	0.652	0.496	0.027		
W5	1890	-0.343	0.075	0.006	0.571	0.438	0.034	20.6	0.3
W5.4	1930	-0.607	0.066	0.007	0.639	0.412	0.046		
W5.6	1970								
W6	1990	-0.536	0.059	0.008	0.608	0.407	0.039	20.1	0.4
W6.4	2030	-0.416	0.066	0.007	0.626	0.345	0.035		
W7	2090	-0.427	0.069	0.007	0.664	0.417	0.025	28.7	0.3
W7.4	2130	-0.372	0.080	0.008	0.547	0.471	0.025		

W8.4	2230	-0.525	0.068	0.007	0.527	0.370	0.033		
W8.8	2270	-0.518	0.068	0.007	0.588	0.316	0.028		
W9.8	2370	-0.433	0.059	0.007	0.553	0.344	0.034		
W10.8	2470	-0.492	0.061	0.006	0.561	0.286	0.039		
W12	2590	-0.425	0.080	0.008	0.576	0.322	0.016		
W13	2690	-0.439	0.059	0.008	0.573	0.233	0.049		

1017

1018

Eastbourne redox sensitive trace metal ratios performed on 0.5 M Acetic acid leachates as in reported in ref. 35. Heights from base of section.						
Sample Name	Height (cm)	U/Ca ( $\mu\text{mol/mol}$ )	Cr/Ca ( $\mu\text{mol/mol}$ )	Ni/Ca ( $\mu\text{mol/mol}$ )	Cu/Ca ( $\mu\text{mol/mol}$ )	V/Ca ( $\mu\text{mol/mol}$ )
GC560	40	0.168	2.442	2.947	2.719	0.953
GC500	100	0.094	2.412	1.371	2.840	0.692
GC440	160	0.174	2.145	1.253	1.573	1.059
GC380	220	0.118	2.115	1.372	2.205	0.766
GC320	280	0.103	2.197	1.381	1.558	0.805
GC260	340	0.123	2.784	2.754	6.432	0.831
GC140	460	0.162	2.318	1.338	3.167	0.890
GC80	520	0.129	2.993	3.446	5.424	0.841
GC200	580	0.163	2.389	1.255	3.196	0.689
PM40	640	0.111	1.556	4.805	6.998	0.888
PM100	700	0.130	1.358	4.855	4.330	0.759
PM160	760	0.088	1.599	4.339	4.842	0.814
PM220	820	0.112	2.093	3.677	5.676	1.193
PM280	880	0.095	1.399	4.259	4.122	0.668
PM340	940	0.078	1.578	3.437	2.102	0.656
PM400	1000	0.070	1.249	1.993	3.738	0.511
PM440	1040	0.063	1.116	1.053	2.310	0.544
PM500	1100	0.092	1.747	1.272	1.858	0.533
PM540	1140	0.112	2.169	3.304	7.983	0.603
PM580	1180	0.118	7.099	23.542	3.919	1.464
PM620	1220	0.093	18.572	24.022	7.000	2.591
PM640	1240	0.052	7.212	2.347	5.434	0.988
PM680	1280	0.183	24.409	24.815	21.766	4.497

PM700	1300	0.083	5.164	1.994	5.227	1.205
PM740	1340	0.086	11.833	7.012	18.659	3.679
PM760	1360	0.058	6.489	2.758	10.789	2.650
PM800	1400	0.083	1.336	1.692	2.592	1.283
W0.4	1430	0.050	3.061	2.287	5.001	0.923
WC200	1440	0.043	0.985	0.754	3.885	0.469
W0.8	1470	0.057	1.055	0.869	5.591	0.764
W1	1490	0.054	0.917	1.225	5.312	0.489
W1.4	1530	0.037	0.891	0.864	3.621	0.266
W1.6	1550	0.036	0.984	1.145	4.553	0.337
W2.2	1610	0.024	0.859	0.713	2.871	0.279
W2.8	1670	0.026	0.833	0.722	3.966	0.305
W3.4	1730	0.030	0.944	0.982	4.669	0.376
W4.2	1810	0.035	1.134	4.042	4.008	0.438
W5.2	1910	0.031	0.883	0.551	3.502	0.387
W5.6	1970	0.058	0.907	0.564	4.186	0.602
W6.4	2030	0.030	0.856	1.914	7.638	0.419
W7.2	2110	0.028	1.013	0.767	3.519	0.449
W7.6	2150	0.021	1.285	0.762	3.872	0.372
W8.2	2210	0.033	0.639	0.566	2.811	0.417
W8.8	2270	0.028	0.765	0.575	2.477	0.318
W9.4	2330	0.030	0.797	0.369	3.255	0.383
W10.6	2450	0.033	0.698	0.618	3.270	0.519
W11.2	2510	0.025	0.616	0.793	2.544	0.366
W11.8	2570	0.030	1.734	0.936	4.600	0.423
W12.4	2630	0.049	5.762	0.953		1.162

1020

1021

1022

Geochemical data for South Ferriby as used in Fig. 1 and S2. Heights from base of section							
Sample Name	Height (cm)	$\delta^{238}\text{Ucarb}$ (‰)	2SE	Mg/Ca (mol/mol)	Sr/Ca (mmol/mol)	Mn/Ca (mmol/mol)	U/Ca ( $\mu\text{mol/mol}$ )
SF-100	0	-0.277	0.060	0.006	0.753	0.813	0.040
SF-90	10	-0.214	0.058	0.006	0.733	0.876	0.048
SF-75	25	-0.122	0.059	0.007	0.741	0.680	0.038
SF-65	35	-0.308	0.057	0.006	0.735	0.816	0.032
SF-55	45	-0.087	0.059	0.006	0.793	0.733	0.048
SF-40	60	-0.099	0.058	0.005	0.778	0.880	0.050
SF-25	75	-0.037	0.058	0.005	0.824	0.831	0.065
SF-15	85	-0.032	0.061	0.006	0.784	0.703	0.055
SF25	125	-0.069	0.060	0.004	0.661	0.845	0.070
SF30	130	0.155	0.066	0.004	0.623	0.964	0.105
SF45	145	0.544	0.058	0.004	0.608	1.016	0.025
SF55	155	-0.161	0.056	0.004	0.660	0.780	0.045
SF60	160	-0.376	0.045	0.005	0.633	0.927	0.024
SF75	175	-0.269	0.052	0.005	0.629	0.963	0.031
SF85	185	-0.342	0.047	0.004	0.663	0.801	0.054
SF95	195	-0.153	0.050	0.006	0.624	0.660	0.051
SF150	250	-0.188	0.064	0.007	0.505	0.721	0.020

1023

1024

Geochemical data for Raia del Pedale as used in Fig. 1 and S2. Heights from base of section. U/Ca presented in Fig 1 are from ref. 35							
Sample Name	Height (cm)	$\delta^{238}\text{Ucarb}$ (‰)	2SE	Mg/Ca (mol/mol)	Sr/Ca (mmol/mol)	Mn/Ca (mmol/mol)	U/Ca ( $\mu\text{mol/mol}$ )
RDP0	0.00	0.280	0.061	0.021	0.350	0.000	2.992
RDP3	3.00	0.081	0.067	0.014	0.207	0.016	1.710
RDP8	8.00	-0.522	0.086	0.769	0.361	0.112	8.902
RDP9	9.00	-0.702	0.070	0.768	0.300	0.029	6.639
RDP16	16.00	-0.872	0.077	0.720	0.360	0.035	11.040
RDP16	19.00	-0.206	0.076	0.017	0.256	0.019	1.272
RDP22.5	22.50	-0.221	0.092	0.017	0.250	0.057	1.323
RDP32	32.00	-0.126	0.073	0.018	0.232	0.032	0.770
RDP33.25	33.25	0.175	0.076	0.016	0.229	0.021	0.729
RDP38	38.00	-0.098	0.070	0.014	0.179	0.004	0.548
RDP39.2	39.25	0.273	0.067	0.015	0.191	0.009	0.407
RDP42	42.00	0.607	0.062	0.011	0.220	0.020	0.463
RDP44	44.00	-0.090	0.069	0.020	0.292	0.032	1.176
RDP51.65	51.65	-0.098	0.070	0.020	0.281	0.011	1.688
RDP56	56.00	0.819	0.079	0.016	0.288	0.006	0.389
RDP59.25	59.25	0.175	0.080	0.020	0.302	0.048	0.764
RDP68.25	68.25	-0.093	0.060	0.019	0.288	0.015	1.028
RDP71.75	71.75	-0.112	0.109	0.012	0.186	0.013	0.501
RDP75.5	75.50	-0.130	0.065	0.021	0.333	0.006	0.856
RDP80.5	80.50	-0.089	0.074	0.014	0.231	0.019	0.547
RDP85	85.00	-0.318	0.085	0.013	0.195	0.019	1.067
RDP89	89.00	0.019	0.062	0.014	0.243	0.042	0.913
RDP97	97.00	-0.210	0.087	0.019	0.252	0.040	1.001